1

Crystal Structure and Phase Transitions in Layered Crystals of Ternary Phosphorous Chalcogenides

1.1 Ferrielectric, Antiferroelectric, and Modulated Orderings in $MM'P_2X_6$ (M – Cu, Ag; M′ – In, Bi; X – S, Se)

Two-dimensional crystals having strong in-plane covalent bonds and weak van der Waals (vdW) interlayer interactions have attracted increasing attention of science community after the discovery of graphene and its interesting properties. Recent years have seen the emergence of relatively new ferroelectric materials belonging to the chalcogenophosphate family [1]. These compounds contain $(P_2X_6)^{4-}$ anions (X = S or Se), which are linked together by cations. Because the ethane-like groups are able to withstand variations in P—P and P—X bond lengths, a large number of chalcogenophosphates have been prepared [2]. Moreover, the coordination preferences of different cations have led to two types of morphologies, i.e. either a three-dimensional or lamellar structure. The nature of dipole ordering derives from bonding, Coulomb, and elastic effects peculiar to a given lattice and may thus be expected to be different in each class. There are six structures representing various cation sublattices possible in this broad class of materials. These include $A_2{}^{2+}[P_2X_6]^{4-}$, $A^{4+}[P_2X_6]^{4-}$, $A_{4/3}{}^{3+}\Upsilon_{2/3}[P_2X_6]^{4-}$ (where Υ represents a vacant site), $A_2{}^{1+}B^{2+}[P_2X_6]^{4-}$, and $A^{1+}B^{3+}[P_2X_6]^{4-}$ (here A and B are metals). The widest variety of symmetries is found within the sulfides. Almost every $A_2{}^{2+}[P_2X_6]^{4-}$-type compound crystallizes into a $C2/m$ monoclinic crystal structure. $Fe_2P_2S_6$ is one of the representative examples for this class of materials. Mixed-cation $A^{1+}B^{3+}[P_2X_6]^{4-}$compounds have more variability in their structure. $AgInP_2S_6$ has a trigonal ($13P_c$) structure and is centrosymmetric at room temperature [3]. Most of mixed-cation compounds are monoclinic. The 2D category is best represented by $CuMP_2S_6$ (M = Cr or In) in which copper is formally monovalent and M is trivalent [4–6]. These compounds consist of lamellae defined by a sulfur framework, which provides octahedral voids for metal cations and P–P pairs. Within a layer, Cu, M, and P–P form triangular patterns. Dipole ordering in these materials requires antiparallel displacements of the d^{10} cations, whereas the copper sublattice is antipolar in $CuCrP_2S_6$ at $T < 150\,K$ [6]. It is polar in $CuInP_2S_6$ below $T_c = 315\,K$ and coexists with the In^{3+} sublattice of unequal and opposite polarity. Cation off-centering is attributable to the second-order Jahn–Teller (SOJT)

Van der Waals Ferroelectrics: Properties and Device Applications of Phosphorous Chalcogenides,
First Edition. Juras Banys, Andrius Dziaugys, Konstantin E. Glukhov, Anna N. Morozovska,
Nicholas V. Morozovsky, and Yulian M. Vysochanskii.
© 2022 WILEY-VCH GmbH. Published 2022 by WILEY-VCH GmbH.

instability associated with the d^{10} electronic configuration; the lamellar matrix absorbs structural deformations via flexible $(P_2X)^{4-}$ groups [4, 5]. Interestingly enough, Sn^{4+} is a d^{10} cation so that off-centering in $Sn_2P_2S_6$ might also be ascribed to a pseudo Jahn–Teller effect.

$CuInP_2S_6$ crystals are an uncommon example of the uncompensated anticollinear two-sublattice ferroelectric system [5]. They exhibit the first-order phase transition of an order–disorder type from the paraelectric to the ferrielectric phase ($T_c = 315\,K$). The symmetry reduction at the phase transition (*C*2/*c* to *Cc*) occurs due to the ordering in the copper sublattice and the displacement of cations from the centrosymmetric positions in the indium sublattice. $CuInP_2S_6$ consists of lamellae defined by a sulfur framework in which the Cu and In cations and P–P pairs fill the octahedral voids and form triangular patterns within a layer (Figure 1.1) [7]. A spontaneous polarization arising at the phase transition to the ferrielectric phase is perpendicular to the layer planes. X-ray investigations have showed that a Cu ion can occupy three types of positions: (i) Cu^1 – quasitrigonal, off-centered positions; (ii) Cu^2 – octahedral, located in the octahedron centers; (iii) Cu^3 – almost tetrahedral, penetrating into the interlayer space [4, 5]. The degree of occupation strongly depends on the temperature [5]. Moreover, two types of positions for Cu^1 are distinguished: Cu^{1u} is displaced upwards from the middle of the layer (centers of octahedrons) and Cu^{1d} is displaced downwards. The ordering of Cu ions (hopping between Cu^{1u} and Cu^{1d} positions) in the double minimum potential is the reason for phase-transition dynamics in $CuInP_2S_6$. At the temperature below T_c (315 K), the intersite copper mobility is limited, trapping the Cu^{1+} sublattice in its displaced state (Cu^1, up) with a compensating shift in the opposite polarity In^{3+} sublattice, resulting in a noncentrosymmetric (*Cc*) ferrielectric phase.

Selenophosphate is other class of materials exhibiting ferroelectric properties. P_2Se_6 bonds have a higher degree of covalence than the P_2S_6 backbone, which is the main difference in this scenario. At low temperature, Cu^+ ion displacement for $CuInP_2Se_6$ is only 1.17 Å [8] compared to 1.58 Å for $CuInP_2S_6$ [5]. This is considered the main cause of the lower phase transitions of the $CuInP_2Se_6$ compound, which include the second-order phase transition at $T_i = 248\,K$ and the first-order phase transition at $T_c = 236\,K$ [9]. The occurrence of incommensurate, quasi-polar phases, in which Cu^+ cation displacement is modulated with a period different

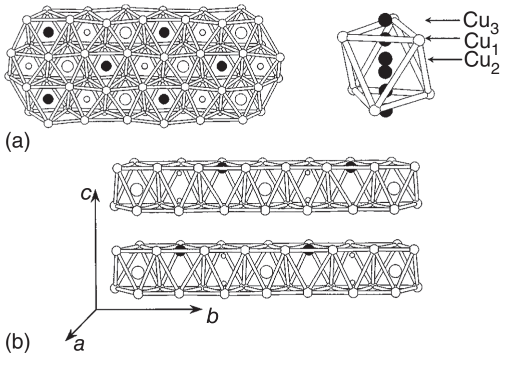

Figure 1.1 (a) Three positions of copper in the cadge. (b) An in-plane view of the layers in the ferrielectric state, Cu shifted up while In shifted down. Source: Maisonneuve et al. [5] / American Physical Society.

from the primary period of the crystal lattice, is attributed to the second-order phase transition in this compound. Other family members show antiferroelectric (AFE) properties. $CuBiP_2Se_6$ and $AgBiP_2Se_6$ are two materials in the selenide family that demonstrate AFE ordering when Bi^{3+} is a trivalent cation [2]. Partially AFE ordering is exhibited in $CuBiP_2Se_6$ below 173 K, with 85% of Cu^+ ions located in the well-defined off-center positions below 97 K. The higher displacement of Bi^{3+} compared to that of In^{3+} could indicate the presence of stereoactive lone pair electrons in Bi^{3+} but not In^{3+}. At room temperature, $AgBiP_2Se_6$ exhibits a similar pattern [2].

Metal and chalcogen substitutions and alloying allow one to efficiently modify and introduce additional functions to the ferrielectric compound $CuInP_2S_6$. As a result, this vital subject has recently received a lot of attention. The typical strategy is to either change one of the two cation sublattices or to modify the P_2S_6 backbone by partial replacement of Se.

1.2 Relaxor and Dipole Glassy States on the Phase Diagram of $CuInP_2(Se_xS_{1-x})_6$ Mixed Crystals

Strongly disordered ferroelectrics such as ferroelectric solid solutions and ceramics can exhibit rather unusual “relaxor” properties among which the most known is a very slow relaxation of polarization. This feature had led to form the “ferroelectric relaxor” notion. Yet, the most important feature of this class of ferroelectric materials is that disorder destroys the ferroelectric transition in them. Thus, in the zero electric field in all temperature range down to $T = 0$, no spontaneous polarization or ferroelectric domains appear in relaxors as well as there are no changes in their (average) crystalline structure. So quite naturally the relaxors have just a broad maximum in the temperature dependence of dielectric susceptibility instead of a sharp peak, and the position of this maximum shifts to lower T at lower frequencies.

Despite the apparent absence of ferroelectric transitions in relaxors, ferroelectric polarization can be generated in them at low T by applying a suitably strong external field for a limited period. Otherwise, one can cool the sample in a strong enough field to a low T and then switch off the field to find that it acquires some polarization that is stable on laboratory time scales. Subsequent heating of the relaxor in the zero field demonstrates that such remanent polarization continues up to the threshold T. For the classical theory of phase transitions, the presence of stable remanent polarization in the material with no ferroelectric transition is a great contradiction and unexplained enigma. Initially, an attempt was made to overcome this dilemma using the concept of “diffuse phase transition,” in which distinct areas of a sample transform gradually into the ferroelectric phase across a temperature interval. This hypothesis appears to contradict X-ray diffraction experiments that show no macroscopic polar areas in relaxors at any T in the zero field [10].

Dielectric materials are electrical insulators that can be polarized by applying an electric field, as opposed to conductors, which carry charges through the materials. When an external electric field is supplied to a dielectric material, the opposite direction field is induced inside the material. The total polarization of the material is the sum of all polarizations relevant to a specific system at the target frequency. It is commonly generated by electronic, ionic, dipolar, and interfacial processes. Orientational glasses are crystalline materials that undergo a transformation from a high-temperature crystalline phase to a low-temperature glassy state. Analogous to the spin glasses (for a review see Ref. [11]), randomly substituted impurity ions that carry a moment are located on a topologically ordered lattice. These moments have orientational degrees of freedom and they interact with one another. The dominant exchange interaction can be of an electrostatic dipolar, quadrupolar, or octupolar, or of an elastic quadrupolar nature. Here the interaction is mediated by lattice strains. The orientational disorder is cooperatively frozen-in as a result of site disorder and anisotropic interactions. The term “glass-state” implies some resemblance to canonical glasses. Indeed, the relaxation dynamics of orientational glasses are similar to those of canonical glasses.

$CuInP_2S_6$ crystals represent an unusual example of the collinear two-sublattice ferrielectric system [5, 12]. Cooperative dipole effects play the main role in these lamellar chalcogenophosphates. The first-order phase transition of an “order–disorder” type from the paraelectric to the ferrielectric phase is observed at $T_c = 315\,K$. The phase transition reduces the symmetry $C2/c \rightarrow Cc$, which occurs due to ordering in the copper sublattice and the displacement of cations from the centrosymmetric positions in the indium sublattice. These results were supported by the Raman investigation of $CuInP_2S_6$ [13]. The spontaneous polarization is perpendicular to the layer planes. These thiophosphates consist of lamellae defined by a sulfur framework in which metal cations and P–P pairs fill the octahedral voids; within a layer, Cu, In, and P–P form triangular patterns [14]. The lamellar structure absorbs structural deformations via flexible P_2S_6 groups while forbidding the cations to antiparallel displacements that minimize the energy costs of dipole ordering. Cu ions can occupy several different positions in the lattice as is shown in Figure 1.2. Cu, In, and P–P form triangular patterns within the layer. Relaxational behavior is indicated by the temperature dependence of spectral characteristics, in agreement with X-ray investigations. It was suggested that a coupling between P_2S_6 deformation modes and Cu^I vibrations enables copper ion hopping motions that lead to the loss of polarity and the onset of ionic conductivity in this material at higher temperatures [13].

1.2.1 XRD Investigations of $CuInP_2Se_6$

The selenium analog $CuInP_2Se_6$ is quite a new addition to this class of chalcogenophosphate materials. Single-crystal XRD investigations were used to clarify the structure of $CuInP_2Se_6$ at various temperatures. $CuInP_2Se_6$ has a lamellar structure like $Fe_2P_2Se_6$ and $Mn_2P_2Se_6$ [15, 16]. Each layer is formed out of one $[P_2Se_6]^{4-}$ unit, and the structures contain well-defined vdW gaps (Figure 1.2).

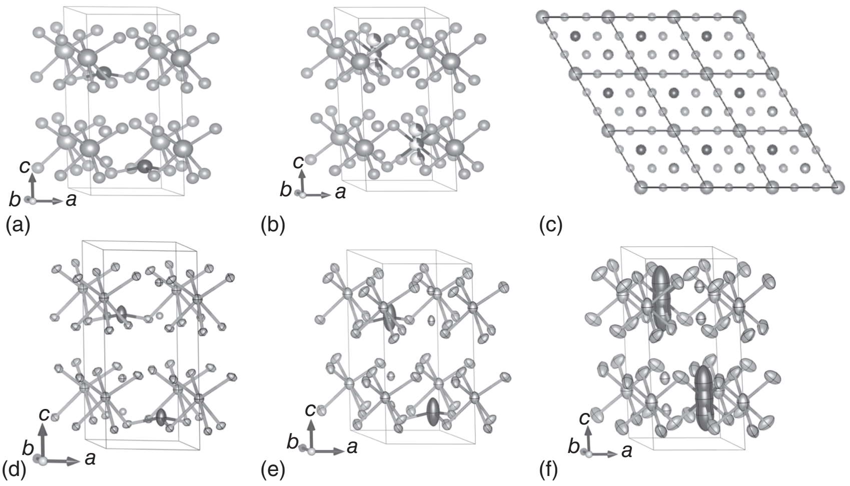

Figure 1.2 Layered structures of $CuInP_2Se_6$ inferred from X-ray diffraction. Structures at (a) 100 K and (b) 293 K. Blue atoms are Cu, pink atoms are In, yellow atoms are Se, and gray atoms are P. (c) View ([001] direction) of a single $CuInP_2Se_6$ layer showing the arrangement of Cu (blue), In (pink), P (gray), and Se (yellow). The atomic displacement of individual atoms of $CuInP_2Se_6$ at (d) 100 K, (e) 180 K, and (f) 250 K.

Full data sets were collected in the temperature range from 100 to 300 K, and the structures were refined using the SHELX-97 software [17]. The refined structural parameters are listed in Table 1.1. The indexing of the diffractograms showed that the phase of $CuInP_2Se_6$ belongs to the noncentrosymmetric space group $P31C$ (No. 159) at 100 and 180 K (Table 1.1a). Therefore, it has a centrosymmetric space group P-31C (No. 163) at 250 K (Table 1.1c). These results largely agree with those of the previous work [8].

Cu^+ and In^{3+} ions in $CuInP_2Se_6$ are octahedrally surrounded by Se atoms, where Cu^+ can occupy a central (more probable) or a near-edge position in the cage (Figure 1.2). The temperature change induces the ordering of Cu^+ in the sublattice of this material. At room temperature, 43% of Cu^+ ions occupy the central position and other 57% are found near the edges of the cage. This indicates copper hoping in the three-well potential at $T > T_c$ and an order–disorder type ferroelectric ordering in $CuInP_2Se_6$. At lower temperature, a probability to find copper located in the middle of the octahedral site decreases. At 100 K, about 93% of the Cu^+ ions are in a well-defined off-center position, displaced by 1.38 Å along the c axis (Figure 1.2d). The remaining 7% of Cu^+ ions are still disordered within the layer as before. In^{3+} shifts in the opposite direction when the temperature is lowered below T_c, by about 0.14 Å at 100 K (Figure 1.2d). Therefore, the material exhibits ferrielectric ordering, similar to that of $CuInP_2S_6$.

It has to be noted that selenides have a higher covalence degree of their bonds compared with that of the sulfide analog. Evidently, for this reason, the copper ion sites in the low-temperature phase of $CuInP_2Se_6$ are displaced only by 1.38 Å from

Table 1.1 (a) Structural parameters of the single-crystal $CuInP_2Se_6$ in the *P*31*C* (No. 159) phase at 100 K. A total of 145 603 reflections are collected. (b) Structural parameters of the single-crystal $CuInP_2Se_6$ in the *P*31*C* (No. 159) phase at 180 K. A total of 14 831 reflections are collected. (c) Structural parameters of the single-crystal $CuInP_2Se_6$ in the *P*-31*C* (No. 163) phase at 250 K. A total of 11 996 reflections were collected.

(a) T = 100 K

a = 6.402(2) Å, c = 13.319(6) Å, and V = 472.8(5) $Å^3$. The agreement factor R_1 = 2.66% was achieved by using 708 unique reflections with $I > 4\sigma$ and the resolution of d_{min} = 0.65 Å. Anisotropic atomic displacement parameters were used for all elements

	Site	***x***	***y***	***z***	**Occupancy**	**U_{eq} ($Å^2$)**
Cu	2*b*	2/3	1/3	0.1474(2)	1	0.0173(4)
In	2*a*	0	0	0.2591(1)	1	0.0087(2)
P_1	2*b*	1/3	2/3	0.3256(3)	1	0.0057(4)
P_2	2*b*	1/3	2/3	0.1579(2)	1	0.0057(4)
Se_1	6*c*	0.3013(1)	0.3228(1)	0.1096(1)	1	0.0069(1)
Se_2	6*c*	0.3552(1)	0.0054(1)	0.3706(1)	1	0.0077(2)

(b) T = 180 K

a = 6.410(8) Å, c = 13.337(20) Å, and V = 474.6(1.3) $Å^3$. The agreement factor R_1 = 4.58% was achieved by using 706 unique reflections with $I > 4\sigma$ and the resolution of d_{min} = 0.65 Å. Anisotropic atomic displacement parameters were used for all elements

	Site	***x***	***y***	***z***	**Occupancy**	**U_{eq} ($Å^2$)**
Cu	2*b*	2/3	1/3	0.1526(4)	1	0.045(1)
In	2*a*	0	0	0.2571(2)	1	0.0136(3)
P_1	2*b*	1/3	2/3	0.3248(4)	1	0.0082(9)
P_2	2*b*	1/3	2/3	0.1587(4)	1	0.0085(9)
Se_1	6*c*	0.3059(2)	0.3248(2)	0.1097(1)	1	0.0119(3)
Se_2	6*c*	0.3531(2)	0.0046(2)	0.3706(1)	1	0.0128(3)

(c) T = 250 K

a = 6.397(1) Å, c = 13.340(5) Å, and V = 472.8(3) $Å^3$. The agreement factor R_1 = 3.80% was achieved by using 538 unique reflections with $I > 4\sigma$ and the resolution of d_{min} = 0.65 Å. Anisotropic atomic displacement parameters were used for all elements

	Site	***x***	***y***	***z***	**Occupancy**	**U_{eq} ($Å^2$)**
Cu^1	2*d*	2/3	1/3	1/4	0.354(6)	0.063(3)
Cu^2	4*f*	2/3	1/3	0.3334(6)	2 × 0.323(6)	0.063(3)
In	2*a*	0	0	1/4	1	0.0217(3)
P	4*f*	1/3	2/3	0.1662(1)	1	0.0133(3)
Se	12*i*	0.33217(8)	0.33730(7)	0.12006(4)	1	0.0211(2)

the middle of the structure layers in comparison with the corresponding displacement 1.58 Å for $CuInP_2S_6$ [5, 14]. Therefore, one can assume the potential relief for copper ions in $CuInP_2Se_6$ to be shallower than for its sulfide analog. Presumably, for this reason, the structural phase transition in the selenide compound is observed at lower temperature than for $CuInP_2S_6$.

The phase transitions in $CuInP_2(S,Se)_6$ crystals are caused by the cooperative freezing of intersite copper motions. This cooperative dipolar behavior is supposed [18] to arise from the presence of an off-centering displacement caused by electronic instability in a form of the SOJT effect related to the d^{10} electronic configuration of cations Cu^+. A SOJT coupling, involving the localized d^{10} states forming the top of the valence band (VB) and the s–p states of the bottom of the conduction band (CB), is predicted to yield such instability. Photoelectron spectroscopy measurements gave the evidence for a strong redistribution of the density of states at the top of the valence band [18]. By combining these data with band-structure calculations, it was shown [18] that these changes are mainly ascribable to the redistribution of the Cu partial density of electron states, related to the off-centered position of d^{10} cations in the ferrielectric phase.

1.2.2 Relaxor Phase in Mixed $CuInP_2(S_xSe_{1-x})_6$ Crystals

Two very similar $CuInP_2(S_xSe_{1-x})_6$ compounds of $x = 0.2$ and $x = 0.25$ are analyzed as they exhibit a peculiar dielectric behavior. Both compositions show just one peak of the real and imaginary part of dielectric permittivity in the temperature range 110–145 K at 10 kHz frequency [19]. A typical dielectric characteristic of relaxor ferroelectrics for both crystals is observed: diffused phase transition without the well-defined Curie temperature. The dielectric permittivity of the $CuInP_2(Se_{0.75}S_{0.25})_6$ crystal is shown in Figure 1.3. A broad peak of $\varepsilon'(T)$ is observed. T_m (peak value of ε') increases with decreasing the frequency of the applied field. A strong dielectric dispersion is detected in the radio frequency region around and below T_m at 1 kHz. The value of T_m (T of the maximum of ε'') is much lower than that of T_m at the same frequency. The position of the peak of $\varepsilon'(T)$ is strongly frequency dependent and no certain static dielectric permittivity is obtained below and around the dielectric permittivity T_m at 1 kHz.

Such behavior can be described by the Vogel–Fulcher relationship

$$\nu = \nu_0 \exp \frac{-E_f}{k(T_m - T_0)}$$

where k is the Boltzmann constant and E_f, ν_0, and T_0 are the parameters the values of which are presented in Table 1.2:

The dielectric dispersion of $CuInP_2(S_{0.25}Se_{0.75})_6$ crystals shows a strong temperature dependence. At higher temperatures, the dielectric dispersion is only in the 10^7–10^{10} Hz region, and on cooling, it becomes broader and more asymmetric. A very broad and asymmetric dielectric dispersion is observed below T_m at 1 kHz. Therefore, the well-known predefined dielectric dispersion formulas, such as Cole–Cole, Havriliak–Negami, or Cole–Davidson, cannot adequately describe the

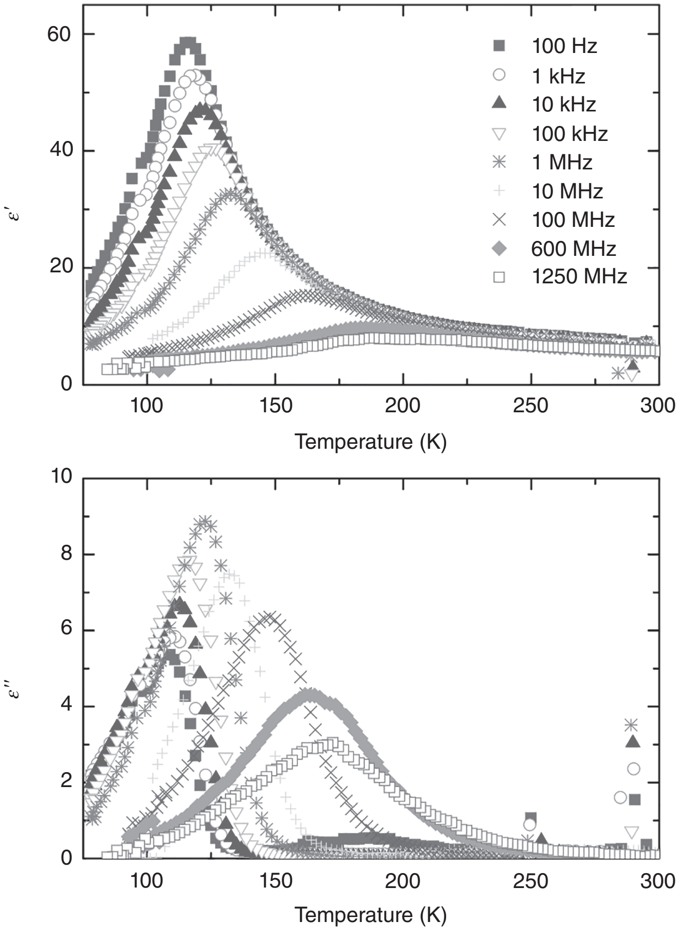

Figure 1.3 Temperature dependence of the complex dielectric permittivity of the $CuInP_2(S_{0.25}Se_{0.75})_6$ crystals measured at several frequencies. Source: Macutkevic et al. [20] / American Physical Society.

dielectric dispersion of the presented crystals. The Cole–Cole formula describes such dielectric dispersion only at higher temperatures due to the predefined symmetric shape of the distribution of relaxation times.

A more general approach must be used for the determination of a broad continuous distribution function of relaxation times $f(\tau)$ by solving the Fredholm integral equations,

$$\varepsilon'(\omega) = \varepsilon_\infty + \Delta\varepsilon \int_{-\infty}^{\infty} \frac{f(\tau)\mathrm{d}(\ln \tau)}{1 + \omega^2\tau^2} \tag{1.1a}$$

$$\varepsilon''(\omega) = \Delta\varepsilon \int_{-\infty}^{\infty} \frac{\omega\tau f(\tau)\mathrm{d}(\ln \tau)}{1 + \omega^2\tau^2} \tag{1.1b}$$

Table 1.2 Parameters of the Vogel–Fulcher fit of the T_m dependence of frequency for the $CuInP_2(S_xSe_{1-x})_6$ crystals with $x = 0.2$ and 0.25.

Composition	ν_0 (GHz)	T_0 (K)	E_f/k, (K)
$CuInP_2(S_{0.25}Se_{0.75})_6$	38.34	96.8	370
$CuInP_2(S_{0.2}Se_{0.8})_6$	10.96	134.5	150

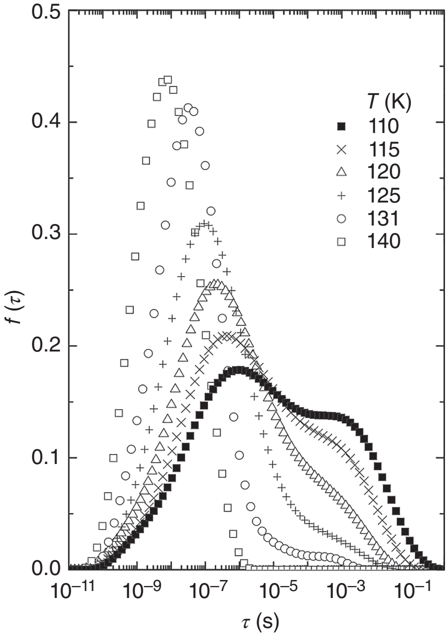

Figure 1.4 Relaxation-time distribution for the $CuInP_2(S_{0.25}Se_{0.75})_6$ crystals at various temperatures. Source: Macutkevic et al. [20] / American Physical Society.

the normalization condition:

$$\int_{-\infty}^{\infty} f(\tau)\mathrm{d}(\ln\tau) = 1 \tag{1.2}$$

The Tikhonov regularization [21] method is applied to solve this equation. The calculated distribution of the relaxation times of $CuInP_2(S_{0.25}Se_{0.75})_6$ crystals is presented in Figure 1.4.

A high-temperature region ($T \gg T_m$) is characterized by a symmetric and narrow $f(\tau)$, while on cooling the $f(\tau)$ becomes broader and more asymmetric so that below T_m (at 1 kHz) the second maximum appears. Such behavior of the distribution of relaxation times has been already observed in the very well-known relaxors: PMN, PMT, and SBN [21–23]. The most probable relaxation time τ_{mp}, the longest relaxation time τ_{max}, and the shortest relaxation time τ_{min} (0.1 level was chosen as sufficiently accurate) have been obtained. The shortest relaxation time τ_{min} is about 0.1 ns for $CuInP_2(S_{0.25}Se_{0.75})_6$ and about 0.01 ns for $CuInP_2(S_{0.2}Se_{0.8})_6$; it increases slowly with the increase in temperature. The longest relaxation time τ_{max} diverges according to the Vogel–Fulcher law. However, the most probable relaxation time τ_{mp} diverges with a good accuracy according to the Arrhenius law. The temperature dependence of the static dielectric permittivity $\varepsilon(0)$ was fitted using the spherical random-bond–random-field (SRBRF) model

$$\varepsilon(0) = \frac{C_{\mathrm{p}}(1 - q_{\mathrm{EA}})}{kT - J(1 - q_{\mathrm{EA}})} + \varepsilon_{\infty} \tag{1.3}$$

where J is the coupling constant and q_{EA} is the Edwards–Anderson order parameter; if $q_{\mathrm{EA}} = 0$, then this equation appears to be the Curie–Weiss law. The Edwards–Anderson order parameter q_{EA} for the relaxor can be determined by the equation [24]

$$q_{\mathrm{EA}} = \left(\frac{\Delta J}{kT}\right)^2 \left(q_{\mathrm{EA}} + \frac{\Delta f}{(\Delta J)^2}\right)(1 - q_{\mathrm{EA}})^2 \tag{1.4}$$

where ΔJ is the variance of coupling and Δf is the variance of random fields. It should be admitted that the equations of the SRBRF model quite well describe the static dielectric properties of the investigated crystals. At sulfur concentrations between $x = 0.25$ and $x = 0.2$, the morphotropic phase boundary between the paraelectric phases $C2/c$ (characteristic of $\mathrm{CuInP_2S_6}$) and P-31c (characteristic of $\mathrm{CuInP_2Se_6}$), or, respectively, the ferrielectric phases Cc and $P31c$ were suggested [19]. Reference [25] using X-ray and Raman investigations confirmed these results later. Notably, the disorder is very high in these compounds, so it can be the reason of the relaxor nature.

1.2.3 Dipolar Glass Phase in Mixed $\mathrm{CuInP_2(S_xSe_{1-x})_6}$ Crystals

$\mathrm{CuInP_2(S_xSe_{1-x})_6}$ crystals with $x = 0.4$–0.9 show no anomaly in static dielectric permittivity, showing that the polar phase transition can be identified even at low temperatures. The dielectric spectra of these crystals are very similar. For example, the real and imaginary parts of the complex dielectric permittivity of $\mathrm{CuInP_2(S_{0.8}Se_{0.2})_6}$ crystals are shown in Figure 1.5 as a function of temperature at several frequencies.

Starting at 260 K and extending to the lowest temperatures, there is a broad dispersion of the complex dielectric permittivity. With an increase in frequency, the maximum of the real part of dielectric permittivity shifts to higher temperatures, as does the maximum of the imaginary part. Such behavior is typical for dipolar glasses. This dispersion is quite well described by the Cole–Cole formula. The temperature dependence of Cole–Cole parameters confirms a typical behavior for dipolar glasses. The mean Cole–Cole relaxation time diverges according to the Vogel–Fulcher law, the Cole–Cole distribution parameter strongly increases on cooling and reaches the value 0.5 below 100 K, and the static dielectric permittivity temperature dependence has no expressed maxima [20]. Usually such behavior is analyzed in terms of the three-dimensional (3D) RBRF Ising model of Pirc [26]. According to this model, the temperature dependence of static dielectric permittivity can be described with Eq. (1.3). The order parameter is defined by the

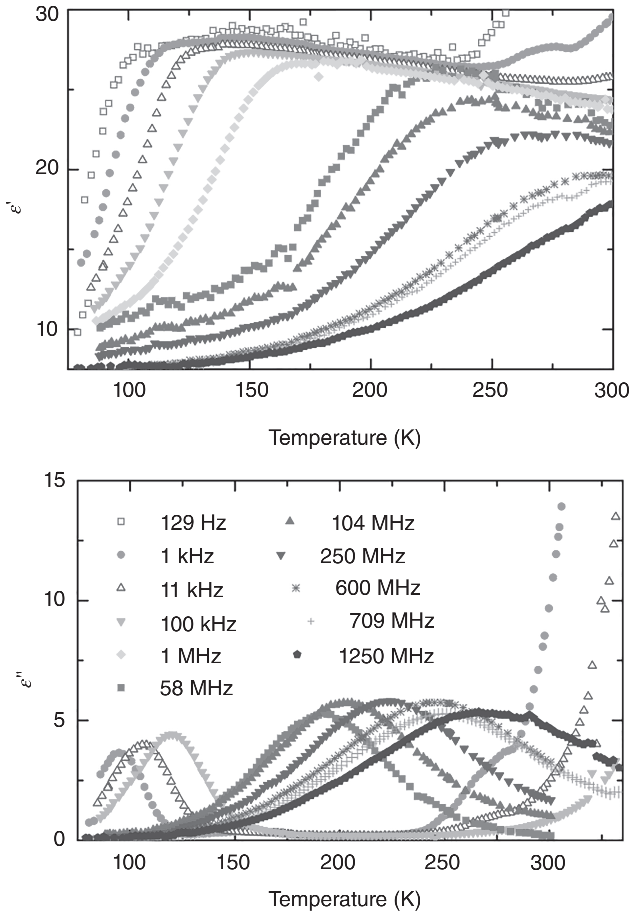

Figure 1.5 Temperature dependence of the complex dielectric permittivity of CuInP$_2$(S$_{0.8}$Se$_{0.2}$)$_6$ crystals measured at several frequencies. Source: Macutkevic et al. [20] / American Physical Society.

two coupled self-consistent equations

$$P = \int_{-\infty}^{\infty} \frac{dz}{(2\pi)^{0.5}} \tanh\left(\frac{\eta}{kT}\right) \exp\left(-\frac{z^2}{2}\right) \tag{1.5}$$

$$q_{\mathrm{EA}} = \int_{-\infty}^{\infty} \frac{dz}{(2\pi)^{0.5}} \tanh^2\left(\frac{\eta}{kT}\right) \exp\left(-\frac{z^2}{2}\right) \tag{1.6}$$

where P is the polarization and

$$\eta = (\Delta J^2 q_{\mathrm{EA}} + \Delta f)^2 z + JP \tag{1.7}$$

Equation (1.3) describes good enough static dielectric properties of the presented dipolar glasses, and the obtained parameters are in a good agreement with the parameters obtained from the Vogel–Fulcher fits, according to the formula [27].

1.2.4 Influence of a Small Amount of Selenium to Phase-Transition Dynamics in $CuInP_2S_6$ Crystals

The dielectric properties of $CuInP_2S_6$ are significantly changed by a small admixture of selenium. The temperature of the main dielectric anomaly shifts from about 315 to 289 K (Figure 1.6). Therefore, the maximum value of the dielectric permittivity ε' significantly decreases from about 180 to 40 (at 1 MHz). Despite that, the peak of dielectric permittivity becomes frequency dependent at higher frequencies (from about 10 MHz) in $CuInP_2(S_{0.98}Se_{0.02})_6$ crystals, and a critical slowing down disappears [28]. An additional dielectric dispersion appears at low frequencies and at low temperatures. The compound with $x = 0.95$ shows qualitatively similar dielectric properties, where the dielectric anomaly with T_c and ε'_{max} shifts to lower values. The dielectric dispersion of the presented crystals is symmetric so that it can be correctly described by the Cole–Cole formula. Again

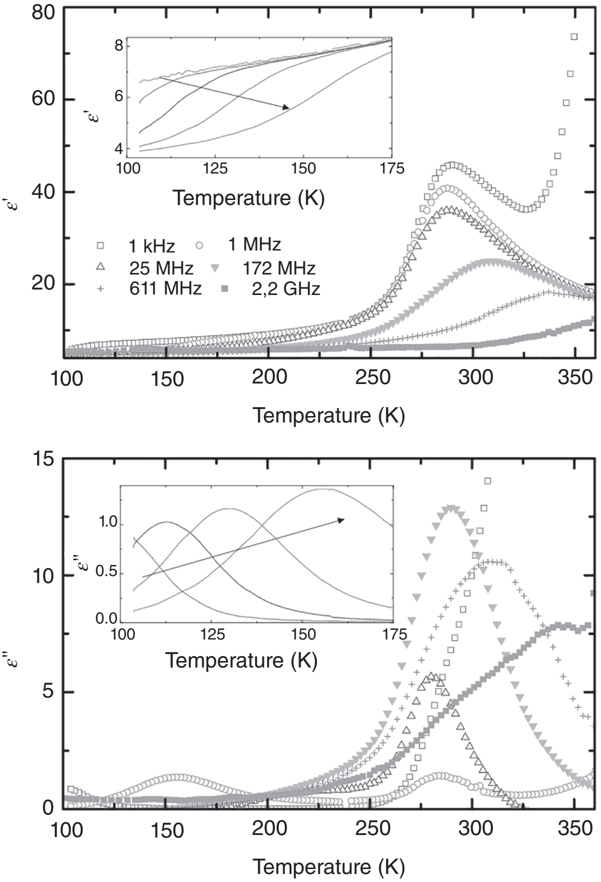

Figure 1.6 Temperature dependence of the complex dielectric permittivity of the $CuInP_2(S_{0.98}Se_{0.02})_6$ crystals measured at several frequencies. Source: Macutkevic et al. [20] / American Physical Society.

Table 1.3 Parameters of the phase-transition dynamics of the $CuInP_2S_6$ crystals with a small admixture of selenium.

Crystal	C_p (K)	C_p/C_f	T_{C_p} (K)	T_{C_f} (K)
$CuInP_2(S_{0.02}Se_{0.98})_6$	8587.7	2.99	137.2	368.7
$CuInP_2(S_{0.05}Se_{0.95})_6$	1906.5	7.01	236.9	282.6

Table 1.4 Parameters of the Vogel–Fulcher fit of the temperature dependences of the mean relaxation times τ_{CC} in $x = 0.98$ and 0.95 inhomogeneous ferroelectrics.

Crystal	τ_0 (s)	T_0 (K)	E/k (K)
$CuInP_2(S_{0.02}Se_{0.98})_6$	8.5×10^{-12}	1150	31
$CuInP_2(S_{0.05}Se_{0.95})_6$	3.77×10^{-11}	1215	28

the distribution of relaxation α_{CC} strongly increases on cooling and reaches 0.43 at low temperatures. The temperature dependence of the dielectric strength $\Delta\varepsilon$ was fitted with the Curie–Weiss law. The obtained parameters are summarized in Table 1.3.

The first-order and order–disorder type of phase transition is determined from the difference $T_{C_p} - T_{C_f}$ and the ratio C_p/C_f. The mean relaxation time τ_{CC} decreases only in a narrow temperature region in the ferroelectric phase and only for $x = 0.98$. Further on cooling, a significant increasing of time τ_{CC} is observed. This increasing is well explained by the Vogel–Fulcher law. These parameters are summarized in Table 1.4.

One can note that all parameters (Table 1.4) for both compounds are close to each other. Such a behavior is very similar to betaine phosphite with a small amount of betaine phosphate [29] and in RADA crystals [30], where a proposition that a coexistence of the ferroelectric order and dipolar glass disorder appears at low temperatures was proposed. Therefore, one can conclude that mixed $CuInP_2(S_xSe_{1-x})_6$ compounds with $x \geq 0.95$ also exhibit the coexistence of ferroelectric order and dipolar glass disorder at low temperatures.

1.2.5 Phase Diagram

For the analysis of phase diagram random bond and random field terms are used. It is assumed that the mean coupling constant J/k is equal to T_C because the Curie–Weiss fit is accurate for these compounds and in this case Eq. (1.3) becomes the Curie–Weiss law. Also for crystals with $x \leq 0.1$, for the same reason it was assumed that ΔJ and Δf are 0. For ferroelectrics with $x \geq 0.95$, ΔJ was obtained from T_0 (Eq. (1.8)), and it was assumed that $\Delta f = 0$. The obtained phase diagram for mixed $CuInP_2(S_xSe_{1-x})_6$ compounds is presented in Figure 1.7.

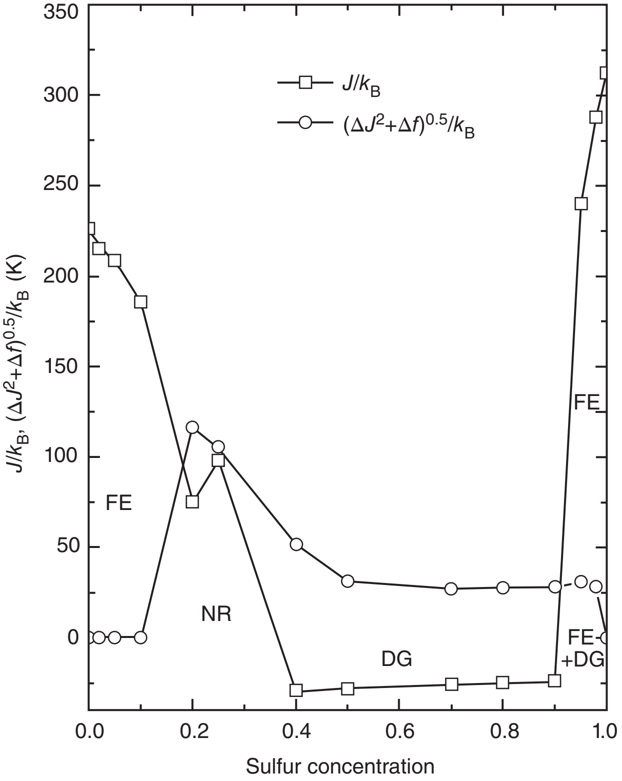

Figure 1.7 Phase diagram of the mixed $\mathrm{CuInP_2(S_xSe_{1-x})_6}$ crystals (FE, ferroelectric phase; NR, nonergodic relaxor phase; DG, dipolar glass phase; FE + DG, ferroelectric and dipolar glass coexistence). Source: Macutkevic et al. [20] / American Physical Society.

For the compounds with $x \geq 0.95$ and $x \leq 0.1$, the mean coupling constant $J > (\Delta f + \Delta J^2)^{0.5}$, therefore, they undergo ferroelectric phase transition at J/k. However, it is a significant difference between the phase-transition dynamics of the mixed crystals with $x \geq 0.95$ and $x \leq 0.1$. In the mixed crystals with $x \leq 0.1$, no any coexistence of the ferroelectric order and dipolar glass disorder is observed down to the lowest temperature (80 K). At temperatures below 100 K, the dielectric permittivity of these compounds is very low (about 3). A low-frequency dielectric dispersion indicates that the crystal splits into domains. Only a decrease of T_C shows that a small amount of sulfur has an effect on the phase-transition dynamics of mixed crystals. The influence of a small amount of selenium to phase-transition dynamics is more significant. Such influence is expressed by a rapid decrease of T_C, the appearance of the ferroelectric and dipolar glass phase coexistence at $x = 0.98$, and the onset of the dipolar glass disorder with x between 0.9 and 0.95. For the crystals with $x = 0.2$ and 0.25, $J < (\Delta f + \Delta J^2)^{0.5}$ and $J \approx (\Delta f + \Delta J^2)^{0.5}$; therefore, the nonergodic relaxor phase appears in these crystals at low temperatures.

In the presence of the external electric field E, the coupling constant J is expected to vary as

$$J(E) = J(0) + \alpha E^2 \tag{1.8}$$

For electrical field E that $J(E) > (\Delta f + \Delta J^2)^{0.5}$ and in mixed crystals the relaxor to ferroelectric phase transition should be observed. The possible existence of the relaxor phase in mixed ferroelectric-AFE crystals is stated in Refs. [31, 32]. No any evidence is indicated for polar nano-region existence in the mixed crystals. The main reason for such phase diagram is that the disorder $(\Delta f + \Delta J^2)^{0.5}$ is highest at $x = 0.2$, where the mean coupling constant is also high enough.

1.3 Antiferromagnetic Ordering and Anisotropy of Magnetization in Multiferroics Cu($In_{1-x}Cr_x$)P_2S_6

Because of their potential uses in information storage, spintronics, and sensorics, multiferroic materials with the coexistence of two or more ferroic orders have gained a lot of attention in recent years. Systems having a long-range polar or magnetic order are typically considered in the quest for these materials. Previously, researchers were more focused on investigating three-dimensional (3D) materials, but they encountered undesirable effects such as dangling bonds and quantum tunneling in nano-scale thin films. Two-dimensional (2D) materials have advantages and are gaining popularity among scientists. Copper chromium thiophosphate $CuCrP_2S_6$ is a promising 2D material with antiferromagnetic (AFM) features caused by the collective ordering of magnetic Cr^{3+} ions and AFE qualities caused by the ordering of Cu^{+} ions. The layered compound $CuCrP_2S_6$ consists of the lamellae defined by a sulfur framework in which the metal cations and P–P pairs fill the octahedral voids [33]. Within the ab planes, the Cu^{+}, Cr^{3+}, and P–P form triangular patterns (Figure 1.8). The monoclinic space group $C2/c$ at room temperature [34]

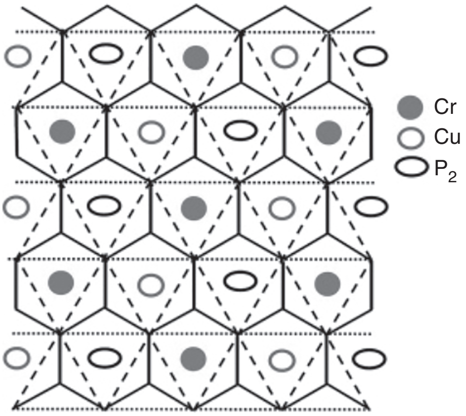

Figure 1.8 Ordered distribution of Cr, Cu, and P_2 pairs in the *ab* plane of (CuCr)P_2S_6. Source: Colombet et al. [34] / with permission of Elsevier.

changes to *Pc* at $T < T_c \approx 150\,\mathrm{K}$ [35]. The Cu^+ positions are AFE ordered, where each layer is separated by a vdW gap and contains rows of Cu^+ ions with alternating up and down shifts along the *c* axis. The mechanism of the ferroelectric transition is of the order–disorder type and involves hopping of the copper ions among two positions in the lattice [33].

The well-known and mostly investigated indium compound $CuInP_2S_6$ (CIPS) belongs to the same *C*2/*c* space group as $CuCrP_2S_6$ at room temperature, but due to a specific SOJT instability of Cu^+ and In^{3+} pairs, it transforms into a ferrielectric structure. Therefore, $CuCr_{1-x}In_xP_2S_6$ with $x > 0$ are of *Cc* symmetry below $T_c \approx 315\,\mathrm{K}$ [35, 36]. These solid solutions are expected to reveal disordered dipolar glass phases with *x* around 0.5 as a consequence of randomness and frustration as confirmed by Ref. [37]. Details of the ferroelectric and dipolar glass phases for $0.4 \leq x \leq 0.5$ were reported in Ref. [38]. Magnetic disorder might also be expected for the magnetic sublattice of solid solutions $CuCr_{1-x}In_xP_2S_6$, where magnetic Cr^{3+} ions (d_3 spin configuration, $S = 3/2$) are randomly replaced by diamagnetic In^{3+} ions. From the literature, it is known that $CuCrP_2S_6$ undergoes AFM phase transition with the Néel temperature $T_N \approx 32\,\mathrm{K}$ [33, 34]. Competing ferromagnetic (FM) intralayer and antiferromagnetic (AFM) interlayer exchange interactions [34] can evoke spin glass phases in the $CuCr_{1-x}In_xP_2S_6$ solutions with $x > 0$. Such coexistence of spin glass with the dipolar glass phase was detected in the layered AFM $Fe_{1-x}Mg_xCl_2$ solid solutions [39, 40].

Both material families of dilute antiferromagnets $CuCrP_2S_6$:In and $FeCl_2$:Mg were compared not by accident. A similar layered structure had been noticed between the lamellar compounds FeX_2 (X = Cl or Br) and transition-metal (M) thiophosphate phases, MPS_3, such as $FePS_3$ [34]. In both materials, the crystalline slabs are separated by vdW gaps, where the layers act as intercalation host material. The analogy becomes clearer when operating the notations $Fe_2P_2S_6$ or stressing the occurrence of P_2 pairs – $[Fe_{2/3}(P_2)_{1/3}]S_2$ [16] and substituting $(Fe^{2+})_2$ for (Cu^+Cr^{3+}). Notwithstanding the above statements, it should be noticed that in contrast to the FeX_2 compounds, even undoped $CuCrP_2S_6$ is a dilute magnet from the beginning (i.e. even in the absence of nonmagnetic In^{3+}), since it always hosts two diamagnetic cation sublattices occupied by Cu and P_2 ions. Extra dilution of the compounds must be considered for understanding the magnetic and magnetoelectric properties discussed below. In fact, the nearest-neighbor Cr^{3+} moments are coupled both in and out of plane by super-superexchange via two S^{2-} ligands [34].

The investigations of magnetic susceptibility χ vs. temperature *T* and the magnetization *M* vs. magnetic field $\mu_0 H$ for In^{3+} contents $0 \leq x \leq 0.8$ revealed dilute antiferromagnetic phases and dynamic spin clustering, but no signs of spin glass behavior as it was expected. Because of this fact the search for multiglass [41] at concentrations $0.4 \leq x \leq 0.8$ is eliminated.

$CuCr_{1-x}In_xP_2S_6$ single crystals were grown by the Bridgman method, and thin samples with typical dimensions of $3 \times 3 \times 0.1\,\mathrm{mm}^3$ were investigated. The *x* and *y* dimensions are defined as *ab*-plane and the height *z* as *c*-axis of the monoclinic crystals [34]. The magnetic easy axis of the $CuCrP_2S_6$ compound lies in the *ab*-plane. However, the spontaneous ferroelectric polarization of the $CuInP_2S_6$ compound is directed perpendicular to the surface [5]. The magnetic measurements were performed using a SQUID magnetometer. For the magnetoelectric measurements, a modified SQUID ac susceptometer [42] was used.

1.3.1 Temperature Dependence of the Magnetization

Figure 1.9a shows the temperature (T) dependence of the magnetization (M) on the $CuCr_{1-x}In_xP_2S_6$ samples with $x = 0$, 0.1, 0.2, 0.4, 0.5, and 0.8 in the external magnetic field of $\mu_0 H = 0.1$ T directed perpendicularly to the ab-plane in the temperature range $5 \leq T \leq 150$ K. It can be seen that M increases with decreasing the temperature and shows cusp-like antiferromagnetic (AFM) anomalies for $x = 0$, 0.1, and 0.2 at $T_N \approx 32$, 29, and 23 K, respectively. The temperature dependence of M above the cusp is well fitted to the Curie–Weiss-type behavior $M \propto (T - \Theta)^{-1}$ [34]. M is found to be almost constant at low temperatures. They remind one of the susceptibility of a uniaxial antiferromagnet perpendicular to its easy axis $\chi_\perp \approx$ const, thus confirming its assertion for $CuCrP_2S_6$ [34]. Bulk $CuCrP_2S_6$ is defined as AFM because the spins are oppositely directed in neighboring layers and it does not matter if the material is in the ferroelectric or in the AFE phase. Once the number of layers is reduced to few-layer nanosheets, the ferromagnetism starts dominating in this material [44]. At very low temperatures, the interlayer AFM interaction is more favored; therefore, it is weaker than the intralayer ferromagnetism.

When $x \geq 0.4$ (at higher In^{3+} concentration), no AFM cusps and any $\chi_\perp \approx$ const is observed, thus confirming its assertion for $CuCrP_2S_6$ [34]. A monotonic increase of M on cooling extends to the lowest temperatures, $T \approx 5$ K. Most obviously, it is because Cr^{3+} concentration falls short of the percolation threshold of the exchange interaction paths between the Cr^{3+} spins.

At higher In^{3+} concentration when $x = 0.8$, the magnetization gains negative values as $T > 60$ K (Figure 1.9a). This peculiarity most probably comes from the diamagnetism of the In^{3+} sublattice where the constant negative magnetization becomes dominant at higher temperatures. For the correct evaluation of the Cr^{3+}-driven magnetism, the diamagnetic background was added to the function showed below:

$$M = \frac{C}{T - \theta} + D \tag{1.9}$$

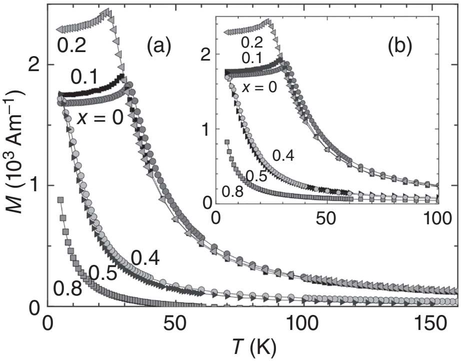

Figure 1.9 Magnetization M vs. temperature T measured on heating on ($CuCr_{1-x}In_x$)P_2S_6 with $x = 0$, 0.1, 0.2, 0.4, 0.5, and 0.8 in $\mu_0 H = 0.1$ T applied parallel to the c^* direction (a) before and (b) after correction for the diamagnetic background. Source: Kleemann et al. [43] / American Physical Society.

Table 1.5 Best-fit parameters of M using Eq. (1.9).

x	θ (K)	C (10^3 A (m K)$^{-1}$)	D (A m^{-1})	Fitting range (K)	R^2
0	30.6 ± 2.1	17.5 ± 1.0	-8.9 ± 5.9	$T \geq 80$	0.9993
0.1	30.4 ± 1.5	16.1 ± 0.3	-6.5 ± 1.5	$T \geq 80$	0.9995
0.2	26.1 ± 1.0	18.4 ± 0.4	-4.6 ± 1.6	$T \geq 80$	0.9994
0.4	15.4 ± 0.3	7.1 ± 0.3	-8.9 ± 0.8	$T \geq 40$	0.9995
0.5	8.5 ± 0.2	7.3 ± 0.3	34.4 ± 0.6	$T \geq 25$	0.9994
0.8	2.5 ± 0.1	3.6 ± 0.3	64.5 ± 0.5	$T \geq 10$	0.9996

It corresponds to the pure Curie–Weiss law with the constant C at sufficiently high temperature and accounts the diamagnetic background for all compositions. The corrected magnetization curves are shown in Figure 1.9b, while Table 1.5 shows the best-fit parameters obtained in individual temperature ranges yielding the highest coefficients of determination, R^2. R^2 exceeds 0.999 for all curves that confirms the suitability of Eq. (1.9). The increasing magnitudes of the negative background values $D \approx -9$, -34, and -64 A m^{-1} for $x = 0.4$, 0.5, and 0.8, respectively, clearly reflect the increasing contribution of diamagnetic In^{3+} ions. Small and nearly constant negative background contributions, $D \approx -6$ A m^{-1}, are noticed for the lower concentrations of In^{3+}, $x = 0$, 0.1, and 0.2. It is very likely that these regularities violate Vagerd's law, which accounts the additivity rule of diamagnetic susceptibilities in compounds and solid solutions [45].

This peculiarity is attributed to an In^{3+}-induced origin of exchange-coupled pairs of Cr^{3+} ions mediated by Cr–S–Cu–S–Cr bridges (Figure 1.8), very similarly as was shown in $CuCrS_2$ [46]. The infinite exchange-coupled cluster maintains the total (positive) additional magnetic moment induced in the connected Cr^{3+} pairs above the bond percolation threshold $p_c = 1x_p = 0.347$ of the triangular lattice of Cr^{3+} ions [47]. As a result, D is kept constant. However, when $p < p_c$ (or $x > x_p$), both the cluster connectivity and the extra moment decay rapidly, resulting in a significant decrease of D, as observed.

This is confirmed by a quite weak initial decrease of the FM (i.e. positive) Curie–Weiss temperatures 31 K > θ, 26 K for $0 \leq x \leq 0.2$, where T_N drops much more drastically (Table 1.5, Figure 1.9). This indicates that the 2D FM interaction within the *ab* planes remains intact, while the interplanar AFM coupling becomes strongly weakened such that T_N decreases considerably. In fact, the interplanar exchange constant, $J_{\text{inter}}/k_B = -1$ K, whose magnitude is not small compared to the FM one, $J_{\text{intra}}/k_B = 2.6$ K [34], is expected to drive the crossover from 2D FM to 3D AFM critical behavior above the potential FM ordering temperature, as confirmed by the higher T_N value compared to θT_N (32.0 K) > θ (30.6 K).

Interplanar AFM bonds become weaker when the diamagnetic dilution is increased (when $x > 0$). Therefore, the Curie–Weiss temperatures achieve positive values, $\theta > 0$, also for high concentrations, $0.4 \leq x \leq 0.8$, the Néel temperatures fall down to zero (Figure 1.10). Obviously, the prevailing exchange interaction remains

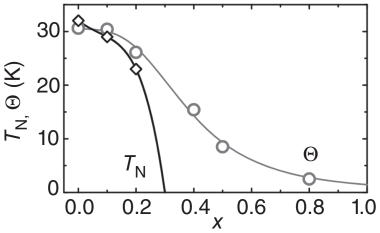

Figure 1.10 Néel (T_N) and Curie (θ) temperatures vs. In^{3+} concentration *x*. Fitted by parabolic and logistic decay curves (solid lines), respectively. Source: Kleemann et al. [43] / American Physical Society.

FM as in the undiluted AFM, $x = 0$ [34]. However, deviations from the linear behavior at low temperatures ($T < 30$ K) indicate that competing AFM interactions favor a disordered structure rather than a pure paramagnetic behavior. Glassy freezing with a nonergodic behavior [46] is not apparent for the $x = 0.5$ compound, as shown in Figure 1.5, because the magnetization data in zero-field cooling/field heating (ZFC-FH) and subsequent field cooling (FC) runs are practically indistinguishable. The In^{3+} concentration x dependences on the characteristic temperatures, T_N and θ, in Figure 1.10 confirm that the compound Cu(Cr$_{1-x}$In$_x$)P$_2$S$_6$ stops being globally AFM at low T for dilutions $x > 0.3$ but continues to show dominating FM interactions even as $x \to 1$. The tentative percolation limit for the occurrence of AFM long-range order as extrapolated in Figure 1.10 is reached at $x_p \approx 0.3$. This is much lower than the corresponding value of Fe$_{1-x}$Mg$_x$Cl$_2$, $x_p \approx 0.5$ [48] Also, differently from the classic dilute antiferromagnet, it was found stronger than the linear decrease of T_N with x. This is probably the result of the dilute magnetic occupancy of the cation sites in the (CuCr)P$_2$S$_6$ lattice (Figure 1.9, [34]), which breaks the intraplanar percolation at lower x than in the densely packed Fe^{2+} sublattice of FeCl$_2$ [48]. A logistic function describes the decay of the Curie temperature in Figure 1.10,

$$\theta = \frac{\theta_0}{1 + \left(\frac{x}{x_0}\right)^p} \tag{1.10}$$

with the best-fit parameters $\theta_0 = 30.4$, $x_0 = 0.385$, and $p = 3.14$. It characterizes the decay of the magnetic 3D long-range order into 2D FM islands, which rapidly accelerates for $x > x_0 \approx x_p$ but sustains the basically FM coupling up to $x \to 1$.

1.3.2 Field Dependence of the Magnetization and Anisotropy of Magnetization and Susceptibility

In the highly dilute regime, $0.4 \leq x \leq 0.8$, the magnetization curves (taken at $T = 5$ K in fields $5\,\text{T} \leq \mu_0 H \leq 5\,\text{T}$) show saturation tendencies. The most pronounced compound is with $x = 0.5$, where spin-glass freezing might be expected as reported, e.g. for Fe$_{1-x}$Mg$_x$Cl$_2$ [48]. However, no indication of hysteresis is detected. Noteworthy, it excellently fits the Langevin-type functions

$$M(H) = M_0[\coth(y) - 1/y] \tag{1.11}$$

where $y = (m\mu_0 H)/(k_B T)$ with the paramagnetic moment m as solid lines, while Table 1.6 summarizes the best-fit results. Since CuCr$_{1-x}$In$_x$P$_2$S$_6$ can also be

Table 1.6 Best-fit parameters of $M(H)$ according to Eq. (1.11).

x	M_0 (kA m^{-1})	m	$N = M_0/m$ (nm^{-3})
0.4	65.7	5.6×10^{-23} A m^2 = 6.1 μ_B	1.2
0.5	59.6	8.5×10^{-23} A m^2 = 6.1 μ_B	0.7—
0.8	24.7	5.6×10^{-23} A m^2 = 6.1 μ_B	0.4

regarded as a quasi-2D FM for Cr^{3+} concentrations below the bond percolation, $p < p_c = 1 - x_p = 0.347$ [47] this interpretation is probably suitable for $x = 0.4$ and 0.5, but should not work for $x = 0.8$. While the saturation of magnetization M_0 and the moment density N scale reasonably well with the Cr^{3+} concentration, $1 - x$, the paramagnetic moments exceed the atomic one, m (Cr^{3+}) = 4.08 μ_B [34] by factors up to 2.5. This is the result of the FM interactions between the nearest-neighbor moments. They become evident at low T and are related to the observed deviations from the Curie–Weiss behavior.

The magnetization analysis of $Cu(Cr_{1-x}In_x)P_2S_6$ compounds revealed an interesting discovery of strong anisotropy, while it is very low in the concentrated compound, (CuCr)PS_3 [34]. The isotropic susceptibility behavior was found for $MnPS_3$, which strongly contrasts with the anisotropic susceptibilities observed on $FePS_3$ and $NiPS_3$ [49]. Magnetic isotropy comes from the orbital singlet states involved $^6A_1$ ($S = 5/2$) for Mn^{2+} in $MnPS_3$ and $^4A_2$ ($S = 3/2$) for Cr^{3+} in $CuCrP_2S_6$. In both cases, the lacking orbital moment makes the spin–orbit interaction marginal and causes virtual insensitivity to the trigonal distortion of the S_6 octahedra to the lowest order. In the case of $Cu(Cr_{0.5}In_{0.5})P_2S_6$, both the isothermal field dependences M vs. $\mu_0 H$ ($\leq$5 T) at T = 5 K (Figure 1.11a) and the temperature dependences M vs. T ($\leq$30 K) for $\mu_0 H = 0.1$ T (Figure 1.11b) split up under different sample orientations. The enhancements by up to 40% were found when rotating the field from parallel ($H_{\parallel}$) to perpendicular ($H_{\perp}$) to the c^* axis. At T = 5 K, it was

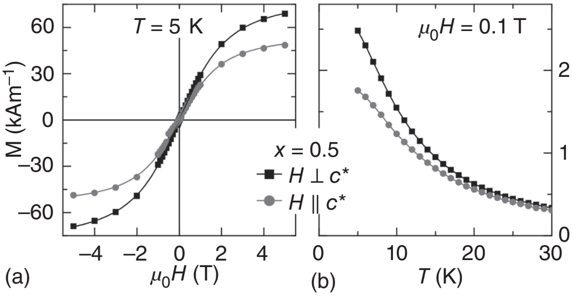

Figure 1.11 Magnetization M of $(CuCr_{0.5}In_{0.5})P_2S_6$ measured parallel (circles) and perpendicularly (squares) to the c^* axis (a) vs. $\mu_0 H$ at T = 5 K (best fitted by Langevin-type solid lines) and (b) vs. T on cooling at $\mu_0 H$ = 0.1 T (interpolated by solid lines). Source: Kleemann et al. [43] / American Physical Society.

observed that $M_\perp \approx 70$ and $2.5\,\mathrm{kA\,m^{-1}}$ vs. $M_\parallel \approx 50$ and $1.8\,\mathrm{kA\,m^{-1}}$ at $\mu_0 H = 5$ and $0.1\,\mathrm{T}$, respectively (Figure 1.11a,b).

This anisotropy effect might just be due to different internal fields, $H^{\mathrm{int}} = H - NM$, where N is the geometrical demagnetization coefficient. Indeed, from the thin sample geometry, $3 \times 4 \times 0.03\,\mathrm{mm}^3$, with $N_\parallel \approx 1$ and $N_\perp \ll 1$, one anticipates ${H_\parallel}^{\mathrm{int}} < {H_\perp}^{\mathrm{int}}$, hence $M_\parallel < M_\perp$. However, the demagnetizing fields, $N_\perp M_\perp \approx 0$ and $N_\parallel M_\parallel \approx 50$ and $1.8\,\mathrm{kA\,m^{-1}}$, are no larger than 2% of the applied fields, $H = 4\,\mathrm{MA\,m^{-1}}$ and $80\,\mathrm{kA\,m^{-1}}$, respectively. These corrections are more than one order of magnitude too small as to explain the observed splitting.

The inherent anisotropy of the paramagnetic centers is examined in the layered $(CuCr)PS_3$ structure as anisotropy emerges in the paramagnetic phase (Figure 1.11b). Consider the anisotropy of the total moments of uncoupled Cr^{3+} ions that undergo orbital momentum transfer to the spin-only ground state. Indeed, the zero-field splitting of the $^4A_2(d_3)$ ground state of Cr^{3+} is expected in the axial crystal field, which admixes the $^4T_{2g}$ excited state via the second-order spin–orbit interaction. The magnetic moment then fluctuates under different field directions as the gyrotropic tensor components, $g_\perp$ and $g_\parallel$, while the susceptibilities follow ${g_\perp}^2$ and ${g_\parallel}^2$, respectively. However, since $g_\perp = 1.991$ and $g_\parallel = 1.988$ [34], the single-ion anisotropies of both M are just 2% effects, unable to explain the experimentally observed anisotropies.

The way out appears to be concealed in the collective nature of the dynamic Cr^{3+} clusters, as single-ion and dipolar-cluster features are unable to solve the anisotropy enigma. It was proposed that they produce molecular magnets with a high spin ground state and substantial magnetic anisotropy [50], similar to the AFM molecular ring molecule Cr_8 [51] because of their intrinsic exchange coupling. In addition to simple 2D FM correlations, the considerably enhanced magnetic moments derived from the Langevin-type fits (Table 1.6) appear to show marginal antiferromagnetic interlayer correlations. Their magnetic moments seem to be partially compensated under this hypothesis.

The dilute antiferromagnets $(CuCr_{1-x}In_x)P_2S_6$ reflect the lamellar structure of the parent compositions in many respects. First, the distribution of magnetic Cr^{3+} ions is dilute from the beginning because of their site sharing with Cu and (P_2) ions in the basal *ab* planes. This explains relatively low Néel temperatures (<32 K) and the rapid loss of magnetic percolation when diluting with In^{3+} ions. Second, at $x > 0.3$, quasi-critical fluctuations involving 2D FM exchange-coupled Cr^{3+} ions mirror the layered structure. They give rise to deviations of the magnetization from the Curie–Weiss behavior at low T and to a strong axial anisotropy reminding of quasimolecular magnetic properties. Similarly, a dynamic polar clustering occurs at $x > 0$ and superposes structural glassiness to the ferrielectric long-range Cu^+ order at low temperatures.

1.4 Magnetic Ordering in $Mn_2P_2S_6$ Crystal

Layered thiophosphates MPS_3 (M = Mn, Fe, Co, Ni, and Cd) crystallize in the monoclinic lattice with a space group $C2/m$, as it was determined by Ouvrard and coworkers [15]. $MnPS_3$ is a vdW crystal with rich physicochemical properties. In particular, its layered structure gives a clear pathway to obtain the 2D material by the exfoliation method [52]. Also, it is worth noting that at 78 K, the $MnPS_3$ crystal undergoes a transition toward a collinear antiferromagnetic phase [53] in which a linear magnetoelectric coupling is allowed. The Mn compounds of the $MnPS_3$ structure are known to exhibit the antiferromagnetic Néel order in a bulk form of the mentioned crystal [54, 55]. Another interesting thing about the $MnPS_3$ crystal is that both magnetic and crystallographic lattices are two dimensional. The $MnPS_3$ layers are separated not by nonmagnetic ones but by a vdW's gap. Exhibiting a high structural anisotropy, the mentioned material can be intercalated by alkali metal ions without any significant distortion of the lattice parameters, making it a promising candidate for the creation of low-cost cathodes for high-energy-density batteries [56]. Recently, the magnetoelectric $MnPS_3$ crystal is also considered as a new candidate for ferrotoroidicity [56]. The hexagonal shape of the 2D sublattice of Mn atoms makes the $MnPS_3$ layered crystal a promising material for the creation of heterostructures built upon this semiconductor and such insulators as graphene or MoS_2 [57]. Du et al. showed that the calculated cleavage energies of $MnPS_3$ are smaller than those of graphite [52]. In Ref. [58], the value of the magnetic moment (μ) of the $MnPS_3$ crystal equal to 5.98 was obtained.

The energy band spectrum of the $MnPS_3$ crystal was for the first time calculated by Kurita within the local-density-functional formalism. In this paper, the authors figured out discrepancies in the calculated and experimental values of the energy gap in the considered crystal. The theoretical calculations of the energy band spectrum [59] do not give a full description of the electronic subsystem of the $MnPS_3$ crystal.

The lattice dynamics of $MnPS_3$ have been never investigated by the ab initio approach. The experimental investigation of infrared and Raman spectra was presented by Bernasconi et al. [60]. Also, in this work, the theoretical investigation of the lattice dynamics of transition-metal phosphorous trichalcogenides was considered by the framework of an axially symmetric force-constant model generated by short-range two-body potentials.

The $MnPS_3$ crystallizes in the base-centered monoclinic lattice with the symmetry of the $C2/m$ space group (No. 16) [15]. The volume of the corresponding primitive unit cell [61] is two times smaller than the volume of the conventional one. The lattice parameters of the conventional unit cell of the $MnPS_3$ crystal (a, b, and c) and the parameters of the primitive unit cell (a_1, a_2, and a_3) are related as follows:

$$a_1 = (a + b)/2, \;\; a_2 = (a - b)/2, \;\; a_3 = c$$

Here $a = 6.077\,\text{Å}$, $b = 10.524\,\text{Å}$, $c = 6.796\,\text{Å}$, $\alpha = \beta = 90°$, $\gamma = 107.35°$, and $a_1 = a_2 = 6.076\,\text{Å}$, $a_3 = 6.796(1)\,\text{Å}$, $\alpha = \gamma = 98.576°$, and $\beta = 119.99(2)°$. The primitive unit cell of $MnPS_3$ contains two formular units ($Z = 2$) (see Figure 1.12).

A structure of the $MnPS_3$ crystal is characterized by parallel planes of transition-metal ions separated by two planes of the sulfur atoms. Six sulfur atoms form a trigonally distorted octahedron surrounding each ion of the transition metal. In the layered $MnPS_3$ crystal, the adjacent planes of sulfur atoms are weakly bonded by the vdW interactions. Each layer in the $MnPS_3$ crystal consists of

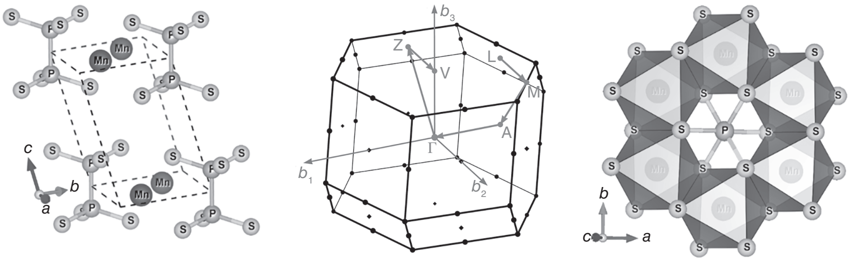

Figure 1.12 Primitive unit cell of the $MnPS_3$ crystal (left) and the corresponding Brillouin zone (middle) with the labels of the special points of high symmetry (V (0, 0, ½), Γ (0, 0, 0), A (½, 0, 0), M (−½, ½, ½), L (−½, 0, ½), and Z (0, −½, ½)) and one layer of this material directed along the c-axis (right).

Mn^{2+} cations and of hexatiohypodiphosphate anions $P_2S_6{}^{4-}$ linked together by the Mn—S bonds [62]. Also, the $MnPS_3$ crystal can be considered as formed by two distinct atomic groups, MnS_6 and P_2S_6, each one with a near-octahedral coordination. The P—S bonds are considered as covalent, while the Mn—S bonds are ionic.

The electronic properties of the $MnPS_3$ crystal under the different orientation of a magnetic moment of the Mn atoms were investigated [63]. The orientation of the magnetic moment for the AFM $MnPS_3$ crystal, as an example, is presented in Figure 1.13. The calculations were performed for the atomic relaxed structure during the geometry optimization procedure. The calculations at the level of geometry optimization and energy calculations were performed applying the DFT/LDA methodology. The computationally obtained results for the NM and AFM $MnPS_3$ crystals are presented in Table 1.7. There α denotes the spin-up electron states and β corresponds to the spin-down electron states. The magnetic moment orientation for

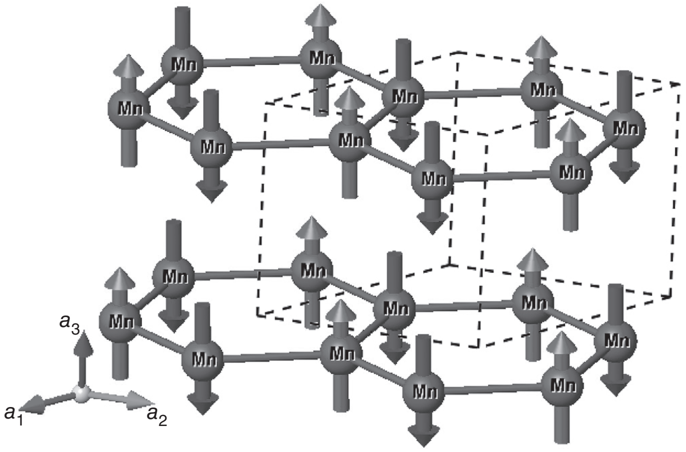

Figure 1.13 Magnetic moment arrangement of the Mn^{2+} atoms in the antiferromagnetic structure of the $MnPS_3$ crystal (AFM $MnPS_3$) with the honeycomb lattice.

Table 1.7 Calculated energy parameters for the ferromagnetic and antiferromagnetic phases of the $MnPS_3$ crystal using the DFT/LDA approach.

State	Mn1	Mn2	μ (Mn1)	μ (Mn2)	E_{tot} (eV)	E_g (eV)	α, β
Nonmagnetic (NM)	5↑	5↑	5.12	5.12	−2754.75	2.23	$\alpha \neq \beta$
Antiferromagnetic (AFM)	5↑	5↓	5.21	−5.21	−2754.78	2.88	$\alpha = \beta$

the $MnPS_3$ crystal was studied experimentally by Kurosawa et al. using the neutron diffraction method [64]. The experimental investigations proved that the $MnPS_3$ semiconductor has a direct bandgap equal to 2.96 eV [65].

Analyzing the data presented in Table 1.7, one may see that the DFT/LDA methodology decreases the energy gap value calculated for both phases of the $MnPS_3$ crystal. In consequence, it was shown that the open d-shells of Mn atoms create the energy state between the valence and the conducting band decreasing the energy gap. The energy properties of the $MnPS_3$ crystal were also investigated applying the DFT/PBE and DFT/HSE06 functional as well as adding the Grimme correction, but any of the proposed approaches does not give the value of the bandgap correlating with the experimental data. The DFT/HSE06 functional drastically decreases the energy gap of the $MnPS_3$ crystal giving its unsatisfactory value equal to 1.23 eV. However, it was shown that applying a combination of the hybrid functional with the Hubbard correction, where $U = 5$ eV, the calculated energy bandgap is equal to 3.05 eV [66].

The quantum chemical calculations of the NM and AFM phases of $MnPS_3$ were performed to determine their magnetic stability. Analyzing the data presented in Table 1.8, one may see that the antiferromagnetic phase is more stable than the nonmagnetic state, but the obtained difference is insignificant. The structural parameters concerning the discussed calculations are also presented in Table 1.8. Comparing the interatomic distances, one may say that the data obtained for the AFM structure are closer to the experimental values than the results reached for the NM structure. In consequence, one may conclude that for future investigations, it is possible to focus on an electronic structure of the AFM phase. One should also notice that the calculations performed in the present work were carried out at $T = 0$ K. The temperature dependence of the $MnPS_3$ energy gap was investigated by Grasso et al. [67]. They show that the bandgap of the mentioned material at low temperature is equal to 2.96 eV. Additionally, it was proved that the DFT-D approach better describes the cleavage energies of MPS_3 (where M = Fe, Mn, Ni, Cd, and Zn) crystals [52]. Therefore, in the present work, the dispersion correction to be also applied for the description of the electronic properties of the AFM $MnPS_3$ crystal is proposed.

In this case, the geometry of the investigated crystal was optimized by a full relaxation procedure using the DFT/LDA methodology with different dispersion correction DFT-D methods (where D means OBS, TS, or Grimme correction). The results of the performed calculations compared with the experimental data are presented in Table 1.8. The structural parameters of the $MnPS_3$ crystal were also calculated in

Table 1.8 The experimentally measured and the theoretically calculated structural parameters of the $MnPS_3$ crystal.

Bond identification	**Bond length (Å)**					
	Exp. (Friedel, Soufre et ses composés – Sur une nouvelle série de sulfophosphures, les thiohypophosphates, 1894)	**DFT/LDA**		**DFT/GGA-D (TS)**	**DFT/LDA-D (OBS)**	**DFT/LDA-D (Grimme)**
		Atomic relaxed structure		**Fully optimized structure**		
		AFM (↑5 ↓5)	**NM (↑5 ↑5)**	**AFM (↑5 ↓5)**		
P1–S2	2.029 65	2.033 58	2.028 11	2.040 24	2.016	2.016
P1–S1	2.034 19	2.037 08	2.035 58	2.041 71	2.017	2.019
P1–P1	2.187 36	2.181 79	2.193 33	2.218 50	2.184	2.192
S1–Mn1	2.621 51	2.583 58	2.641 67	2.710 53	2.621	2.607
S2–Mn1	2.594 77	2.594 77	2.637 62	2.701 41	2.619	2.606
a	6.076			6.235	6.038	5.995
b	6.076			6.235	6.038	5.995
c	6.796			7.175	6.915	6.652
$\alpha = \gamma$ (°)	81.42			81.754	81.848	81.646
β (°)	119.99			119.998	120.003	119.984
V (Å^3)	207.43			231.38	209.44	198.19
E_{tot} (eV)	—			−2754.00	−2754.68	−2754.58
E_g (eV)	2.92			2.81	2.58	2.46

the work [66], but the authors do not show the impact of different types of dispersion corrections on the structural parameters of the studied material. In this case, to the best of our knowledge, the presented work is the first one reporting these calculations. The proposed type of calculation is very important for the investigation of vibration properties of the $MnPS_3$ crystal.

Analyzing the data collected in Table 1.8 and comparing them to the experimental results, one may see that the best $MnPS_3$ structure was theoretically obtained using DFT/LDA-D(OBS) methodology. In this case, the calculated lattice parameters are close to the experimental data. Also, the total energy of the fully optimized $MnPS_3$ structure is the lowest one when the DFT-D(OBS) correction is used. It means that the structure optimized by DFT/LDA-D(OBS) methodology is energetically more favorable.

Although the values of the structural parameters close to the experimental results were obtained when the calculations were carried out by DFT/GGA-D(TS) methodology, in this case, the optimization of the structure was not properly correct. In view of the fact that the $MnPS_3$ crystal is characterized by the vdW bandgap, the distance between the layers of Mn atoms was tested. The performed calculations show that the distance between the mentioned layers of the crystal is equal to $d_{\mathrm{Mn-Mn}} = 7.174\,\text{Å}$ with reference to the experimental value $d_{\mathrm{exp}} = 6.796\,\text{Å}$ [15]. It means that the calculated distance increases by about 40% with respect to the experimental data, which cannot be accepted. The interlayer distance in the $MnPS_3$ crystal was also measured by Yagotintsev et al. using X-ray diffraction as a function of temperature in the vicinity of the Néel point at 78 K [68]. There it was found that temperature drop decreases the interlayer distance. At 40 K, the distance between Mn layers is equal to $d_{\mathrm{exp}} = 6.474\,\text{Å}$. It was additionally proved that the fully optimized $MnPS_3$ crystal structure using DFT-D(TS) correction cannot be accepted.

As a result of the performed calculations, it was found that the DFT/LDA-D(OBS) methodology is the best one properly describing the geometry of the considered crystal, but any of the applied methods do not reproduce correctly the values of the bandgap with reference to the experimental data. Therefore, the Hubbard correction was proposed to be applied. These calculations were carried out by two methods: first, initially the unit cell of the considered material was fully optimized by DFT/LDA-D(OBS) methodology, and after this, the Hubbard parameters for the d-orbitals of Mn atoms were included for the calculations of electronic properties. The second method involves including the mentioned Hubbard correction from the step of the geometry structure optimization. The added Hubbard correction parameter was equal to $U = 2.5\,\text{eV}$. Comparing the results of these calculations, any significant differences in the energy band structure were observed. The results of energy-band-structure calculation for the AFM $MnPS_3$ crystal using the first approach (DFT/LDA-D(OBS)) are presented in Figure 1.14. The calculated energy gap equal to 2.88 eV is in good agreement with the experimental data [65].

To explain the influence of the Hubbard parameter on the electron system of the $MnPS_3$ crystal, the partial density of the state (pDOS) of Mn, P, and S atoms

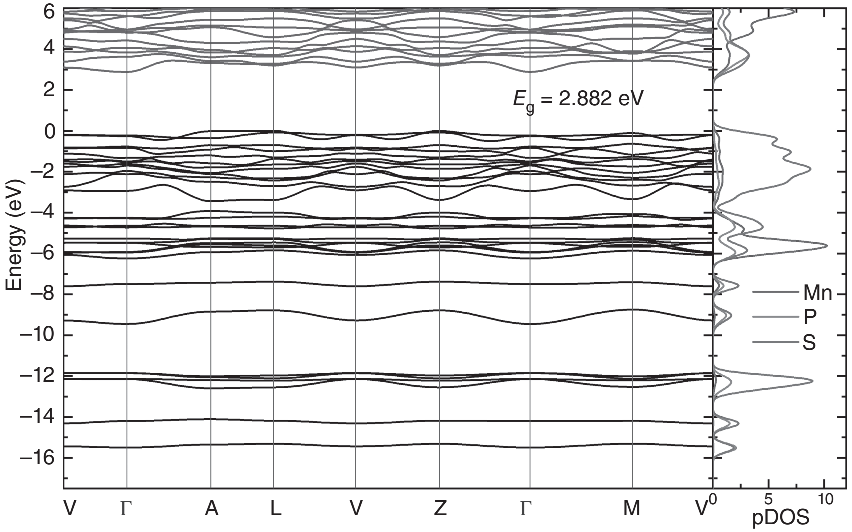

Figure 1.14 Energy band structure of the $MnPS_3$ crystal calculated by DFT/LDA-D(OBS) methodology applying the Hubbard correction at the level of energy calculations.

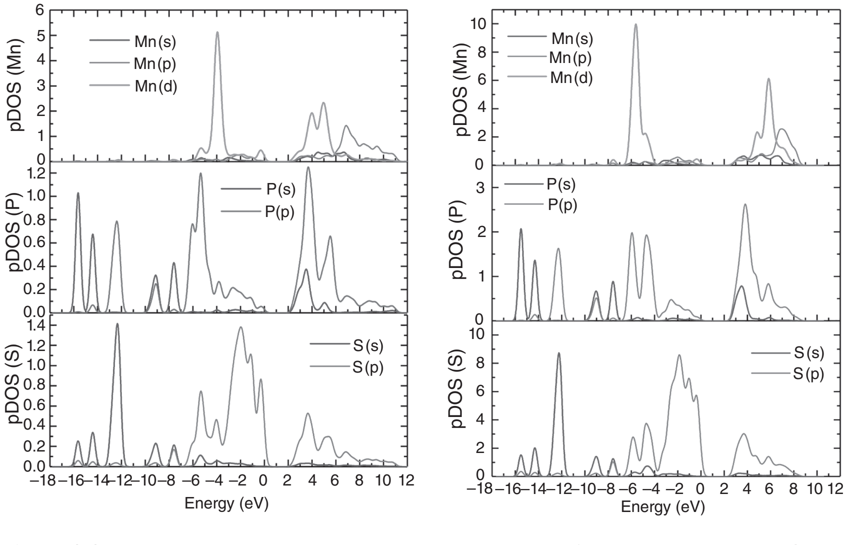

Figure 1.15 Partial density of the state calculated for the AFM phase of the $MnPS_3$ crystal by DFT/LDA-D(OBS) (left) and DFT/LDA-D(OBS) + U (right) methodology.

using DFT/LDA-D(OBS) and DFT/LDA-D(OBS) + U approaches was calculated (Figure 1.15).

According to the electronic configuration of the Mn, P, and S atoms, an energy band structure of the AFM $MnPS_3$ crystal is built of 30 dispersion curves doubly degenerated due to inversion symmetry. The valence band ranges from −16 up to 0 eV and can be decomposed into eight subbands separated by energy gaps. The lowest subband (−16÷−15 eV) is built of the 3s- and 3p-orbitals of sulfur and the 3s-orbitals of phosphor atoms. Next subband, lying in the energy region −15÷−13.5 eV, consists of the 3s-orbitals and 3p-orbitals of both sulfur and phosphor atoms. The third subband has a strong contribution of the S 3s-states mixed with a slight contribution of the 3p-states of phosphor atoms. These first three subbands correspond to the localized electronic states involved in the binding of the [P_2S_6] anion complexes of the considered structure. The energy branches in the −10÷−8.5 eV region, also being a mixture of S 3s, P 3s, and P 3p-orbitals, form the antibonding P—S and bonding P—P states. A weakly dispersive fifth energy branch located in the −8÷−7 eV range is formed by an equal contribution of S 3s and S 3p-orbitals mixed with P 3s, Mn 3d, and Mn 4p-states. This subband represents antibonding P—P states and weak bonding states between neighboring [P_2S_6] complexes through overlapping with Mn orbitals. Next two energy subregions (−6.5÷−5 eV and −5÷−3.9 eV) are mainly formed by an equal minority of the 3p-orbitals of sulfur and phosphor atoms and a strong admixture of Mn 3d-states. The states in the mentioned subbands are responsible for the chemical bonding in the MnS_6 polyhedra. The last valence subband (−4÷0 eV) is formed by comparable contributions of the P 3p, Mn 3d, Mn 4s, and Mn 4p-states adding the major admixture of the S 3s-orbitals. It is worth noting that the dispersion of energy curves in the layered $MnPS_3$ crystal is mostly caused by the peculiarity of its structure. The dispersion of energy branches is rather weak in the direction across the vdW gap (Γ–V) and is significant in the layer plane directions (Γ–A, Γ–M). However, in the last valence subband, we can find energy branch (see Figure 1.14) having an anomalous high dispersion in the Γ–V direction. The mentioned high dispersion means a considerable overlapping between wave functions and in this particular case should have a consequence in the bonding of interlayers.

Comparing the pDOS (Figure 1.15) calculated using the Hubbard correction (right) with that performed by the pure DFT/LDA-D(OBS) methodology (left) in the energy range −4÷−8 eV, the splitting of the single peak was observed. These energy states correspond to the bonding and antibonding states formed by the hybridized sulfurs and phosphorous p-orbitals. An increase in the energy distance between these states corresponds to an increase in the ionicity of the chemical bonding. The same situation for the $Sn_2P_2S_6$ crystal was observed. The opposite situation in the 5 eV energy region is observed. Here the overlap of peaks formed by d-orbitals of the manganese atom is seen.

For a more detailed understanding of the charge interaction between the considered atoms, the total electron density distribution was calculated using the DFT/LDA-D(OBS) + U methodology (Figure 1.16). The obtained results clearly demonstrate that the $MnPS_3$ crystal possesses a covalent-ionic bonding character. However, the P–P and P–S interactions are characterized by covalent bonds. The Mn atoms and P_2S_6 anion complex are connected by ionic bonds.

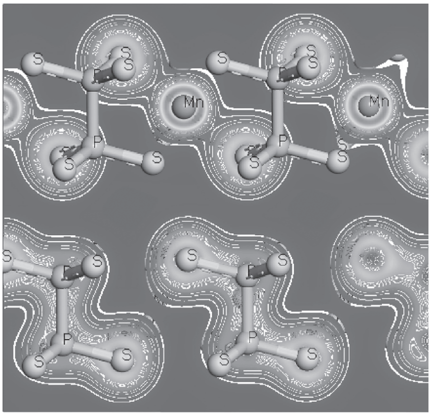

Figure 1.16 Total electron density distribution calculated by DFT/LDA-D(OBS) + *U* methodology for the $MnPS_3$ crystal.

Table 1.9 The Mulliken charges calculated for the $MnPS_3$ crystal by using DFT/LDA-D(OBS) + *U* methodology ($U = 2.5$ eV for the d-orbitals of Mn atoms).

Ions	s	p	d	Total	Charge	Spin
P_1	1.46	2.97	0	4.43	0.57	0
S_1	1.87	4.54	0	6.42	−0.42	0
S_2	1.87	4.55	0	6.42	−0.42	0
Mn_1	0.49	0.68	5.14	6.31	0.69	5.21

Also, the Mulliken charges for the considered crystal were calculated applying the DFT/LDA-D(OBS) + *U* methodology. The results of the mentioned simulation are presented in Table 1.9.

Analyzing these results, one may see that the initial electronic configuration of the Mn atom ($3d^5 4s^2 4p^0$) undergoes the strongest changes in the case of the chemical compound formation. The recharging of Mn 3d and the occupation of an initially empty Mn 3p-orbital obviously prove a strong hybridization between the Mn states and the molecular orbitals of strongly bonded $[P_2S_6]$ complexes. A strong indirect interaction between the electronic shells of manganese atoms by means of the $[P_2S_6]$ complexes states is based on the correlation of magnetic moments and, evidently, it is the driving force for antiferromagnetic ordering in this system.

An implemented appropriate procedure to calculate correctly the electronic properties of the $MnPS_3$ crystal enables us to describe its vibrational properties. The dynamic properties of the mentioned crystal will be discussed in the Chapter 4.

1.5 Polar Layered Crystals of SnP_2S_6 Type

Phosphorus-containing chalcogenide materials of $MM'P_2S(Se)_6$ type with M and M′ transition metals in the cation sublattice possess a layered crystal structure. For the case of Sn and Pb cations from the main subgroup, the phosphorus-containing chalcogenides can crystallize in a three-dimensional lattice (e.g. crystals of the $Sn(Pb)_2P_2S(Se)_6$ system) or in a layered crystal lattice (the unique case of SnP_2S_6). These materials demonstrate different types of dipole ordering (ferroelectric, ferrielectric, AFE, incommensurate modulated, relaxors, and dipole glass), various magnetic ordering, and multiferroicity. Application of these materials opens wide new functionalities.

Earlier, for the $CuInP_2S_6$ crystal from the vdW family with ferrielectric ordering below $T_c \approx 315\,K$, the possibility of spontaneous polarization switching in the samples with a thickness of several structural layers was discovered [69, 70]. This discovery opened a new topic of basic and applied research in the field of nanoelectronics based on vdW multiferroics. By now, numerous examples of functional elements including $CuInP_2S_6$ crystal monolayers or layered sandwiches have been designed. A ferroelectric diode based on $CuInP_2S_6$ demonstrates nonvolatile memory and indicates the possibility of integration with well-established silicon technologies [70]. A $CuInP_2S_6$/germanene heterostructure, for which a change in the direction of spontaneous polarization induces a semiconductor–metal transition, can be used in the development of nonvolatile ferroelectric switches and memory devices [71]. Ferroelectric field-effect transistors were implemented in $CuInP_2S_6$–MoS_2 heterostructures [72–74]. An ultrathin ferroelectric tunneling junction based on a graphene/$CuInP_2S_6$ monolayer/graphene vdW heterostructure exhibits the tunneling electric resistance effect where the tunneling current strongly depends on the direction of ferroelectric polarization [75]. Layered $CuInP_2S_6$ crystals can also be used as nano-scale coolers based on the electrocaloric effect [76].

The functionality of vdW heterostructures can be improved by involving polar metals because a thin enough polar metal could be sufficiently penetrated by an electric field to have its polarity switched [77]. For the crystals of the $Sn(Pb)_2P_2S(Se)_6$ system, a semiconductor-to-metal transition can be induced by high pressure [78], but under compression, their structure becomes centrosymmetric [8, 79]. Taking into account the centricity of the crystal structure at normal conditions, it seems promising to search for the polar metal state in the family of phosphorus-containing chalcogenide compounds.

Ferrielectric polarization of the monoclinic layered $CuInP_2S_6$ crystal is determined by the opposite shifts of Cu^+ and In^{3+} cations out of structural layers that are built by $(P_2S_6)^{4-}$ anionic structural groups and can be related to the SOJT effect destabilizing the Cu^+ cations in the positions in the middle of structural layers [8]. In the case of the $Sn_2P_2S_6$ crystal with a monoclinic three-dimensional lattice, the ferroelectric ordering below $T_c \approx 337\,K$ is also related to the SOJT effect that is based on the specific chemical bonding for the Sn^{2+} cations [80, 81]. Earlier it was found [82] that doping with Ge shifts the ferroelectric second-order phase transition in $Sn_2P_2S_6$

crystals toward higher temperatures. The germanium impurity in $Sn_2P_2S_6$ improves the stereoactivity of the doubly charged cation sublattice and shifts the ferroelectric second-order phase transition toward higher temperatures [82]. The partial substitution of lead by germanium induces polar ordering below 70 K in the quantum paraelectric state of the $Pb_2P_2S_6$ compound [83].

Tin hexathiophosphate SnP_2S_6 has a layered rhombohedral structure R3 (Figure 1.17) that is composed of nonstereoactive Sn^{+4} cations and $(P_2S_6)^{4-}$ anions [84]. This crystal structure lacks half of the metal ions compared to the parent $Sn_2P_2S_6$ structure. The packing of structural layers determines the acentricity of the SnP_2S_6 crystal lattice.

The absence of an inversion center in this crystal appears to be an illogical result: if in $Sn_2P_2S_6$ the nature of the acentrical environment of a Sn atom may be determined by the presence of the lone pair on a Sn^{2+} cation [8], then in the case of SnP_2S_6 one should expect a highly symmetric octahedral coordination for a fully ionized Sn^{4+} cation in the environment of sulfur atoms. However, such an environment has not been found, even at high temperatures. In connection with this, investigations [85] of the structural, dynamical, and electronic properties were performed in the range up to 35 GPa in the framework of the density functional theory in the LDA approximation. Also, the experimental dependence of the SnP_2S_6 lattice vibration frequencies was found by Raman spectroscopy under hydrostatic pressure.

The main objective of these theoretical and experimental studies is to gain a deeper insight into the electronic and vibrational properties of layered semiconductors, because the use of external pressure opens up new possibilities for controlling the anisotropy of chemical bonding. The presence of a vdW gap leads to a different behavior of inter- and intralayer interactions. Beyond a certain pressure, these differences become less pronounced. Therefore, applying external pressure, it becomes possible to investigate the peculiarities of the physical properties of the material in two-dimensional (2D) and three-dimensional (3D) structure morphology.

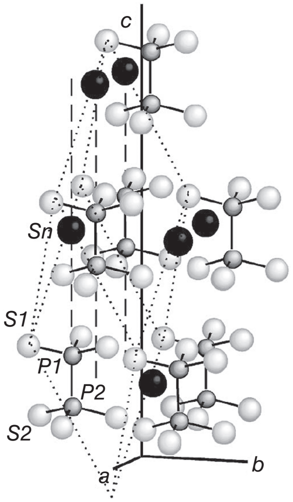

Figure 1.17 Spatial view of the crystal structure of SnP_2S_6. The primitive rhombohedral unit cell is indicated by dotted lines. The hexagonal unit cell (indicated by lattice parameters *a*, *b*, and *c*) contains three primitive rhombohedral unit cells. Vertical dashed lines indicate the three-layer packing in the directions of weak bonding.

The dependence of all principal crystallographic parameters has a monotonic behavior within the pressure range under study (Figure 1.18). The structural parameters are a useful indicator of phase transitions: since no anomalies in the pressure dependence of structural parameters are found for this crystal, we can suppose that the SnP_2S_6 crystal structure does not undergo any collapses or significant distortions, at least up to 35 GPa within the rhombohedral space group $R3$ symmetry constraint. This statement indirectly agrees with the experimental studies of the optical absorption spectra in a wide temperature range [86], which also indicate the absence of structural changes in this crystal. Also, the stable phonon modes rule out a displacive phase transition driven by a phonon instability under pressure.

Interesting peculiarities are observed at pressures of about 5 and 18 GPa. At the former pressure, the Sn–S interatomic distances become equal (cf. Figure 1.18b); at the latter pressure, the same is observed for the P–S distances (cf. Figure 1.18c). At a pressure above 5 GPa, the Sn atom starts to be displaced in the direction of the S2 atoms, while at lower pressures, it is displaced in the direction of the S1 atoms. Such behavior appears to be strange since the Sn displacement toward the S1 atoms at low pressures may be explained by the Coulomb repulsion between the positively charged Sn and P ions, belonging to different layers. At high pressures, this interaction ought to increase due to Sn–P distance shortening, so one could expect the increase of the Sn-atom displacement in the direction of the S1 atoms. But in the case considered here, the opposite behavior is observed: up to 5 GPa, the displacement of the cation from the center of the sulfur octahedra is decreasing with increasing the pressure. Right at the pressure of 5 GPa, the cation is located in the center of the octahedra, and at higher pressures, it is displacing in the direction of the S2 atoms. The P1–S1 and P2–S2 distances are observed to be equal at 18 GPa pressure, while the Sn–S2 distances become considerably different at this pressure. Moreover,

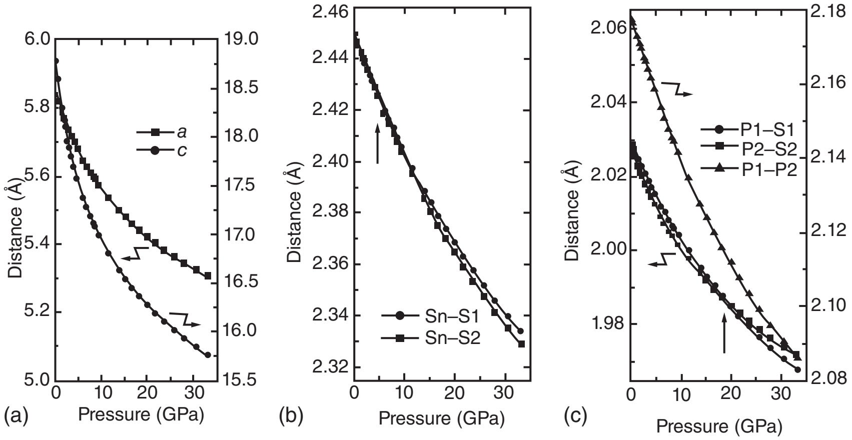

Figure 1.18 Pressure dependence of the main crystallographic parameters. (a) Lattice parameters in the hexagonal crystallographic setting; (b) cation interatomic distances; (c) anion interatomic distances. Vertical arrows indicate the position of the equality of interatomic distances. Source: Rushchanskii et al. [85] / American Physical Society.

the local symmetry of the cation and anion complexes does not contain the inversion operation, even at the mentioned hydrostatic pressures. The reason is that the anion distorts the structure by rotations of the PS3 pyramids around the P–P axis. This distortion is the actual reason for the displacement of Sn in the direction of the nearest-layer P—P bond at high pressures.

To investigate the pressure dependence of structural polarization, calculations of the polarization in the *c* direction have been made [85]. The ground-state polarization is computed by the Berry phase method [85]. Since the pressure dependence of the total polarization pointed to a nonlinear behavior, we have extended the investigations to the pressure range up to 80 GPa. The results are presented in Figure 1.19. The ionic phase has a nonmonotonic behavior, reaching a maximum at ~2 GPa, and from then on its behavior is almost linear, crossing the zero point at ~41 GPa. The almost linear dependence of the ionic phase above 2 GPa corresponds to the above-described monotonic transformation of the asymmetry of the local anion and cation environments. At 41 GPa, the lattice structure is significantly deformed, and the ionic part of polarization disappears as a result of accidental coincidence of the "center of mass" of the anion and cation sublattice.

However, the resulting total polarization at 41 GPa does not disappear due to the presence of its nonzero electronic part. In contrast to the ionic phase, the pressure dependence of the electronic polarization has two extrema. The first one is a minimum, reached at ~7 GPa, where the transition to the direct-gap situation is observed. The vanishing of the electronic part of the Berry phase at ~35 GPa results from a strong interaction between iso-symmetrical electronic states, which form the bottom of the CB and the top of the valence band (VB). At this pressure, the electronic state of the top of VB is formed by orbitals, mainly localized on the anion group, and the bottom of CB is formed by cation group orbitals. The cross-splitting of two states leads to the delocalization of the corresponding wave functions in the space between anion and cation groups and to the corresponding vanishing of the electronic part of the polarization at ~35 GPa. The electronic phase reaches its maximum at ~65 GPa, and then it decreases suddenly. As shown in Figure 1.19, the resulting polarization is nonzero up to ~70 GPa, but even at such a high pressure its

Figure 1.19 Total polarization (in a.u. of charge/Bohr^2) of SnP_2S_6 in the direction of weak bonding as a function of pressure. The ionic and electronic parts of the Berry phase are also shown.

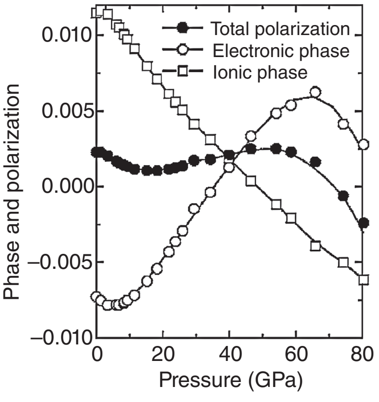

disappearance is the result of the cancellation of two nonzero electronic and ionic components with opposite signs [85].

The first-principles studies of the dynamical and electronic properties, and their pressure dependence of SnP_2S_6 were performed [85]. The lattice vibration eigenvectors have been thoroughly studied. For example, a mixed character of the vibration at ~374 cm^{-1}, which corresponds to the experimental value of ~380 cm^{-1}, has been obtained. The A-symmetry mode at 374 cm^{-1} is formed by the out-of-phase displacements of the P atoms, accompanied by the liberations of the P1–S13 pyramids and breathing of the P2–S23 pyramids. The A-symmetry mode at 443 cm^{-1} is formed by the in-phase oscillations of the P–P atom pairs moving out of phase with all Sn atoms. Both by theory and Raman spectroscopy, the pressure influence does not cause mode softening, at any rate within the BZ center. Also, the theoretical phonon dispersion curves do not indicate mode softening over the entire range of BZ.

The values of the Born effective charges are in a good agreement with their nominal quantities, indicating saturation of the chemical bonds. The electron density distribution confirms the presence of the vdW gap between the neighboring layers of the SnP_2S_6 structure. The presence of the electron density in the cation region and the corresponding orbitals in the valence part of the spectrum indicates that the cation static charge does not achieve the maximum value of +4. The electronic band structure in the principal directions of BZ and its pressure dependence have been investigated [85]. The indirect character of the optical absorption and the transition into the direct bandgap structure of the spectrum at pressures above 10 GPa have been determined. It has been shown that the bottom of CB is formed by the cation localized states, participating in the low-frequency optical lattice vibrations, with which the exponential dependence of the absorption coefficient may be connected, even at liquid nitrogen temperatures.

The family of phosphorus-containing $MM'P_2S(Se)_6$ chalcogenide materials with including promising layered ferrielectric $CuInP_2S_6$ and three-dimensional ferroelectric $Sn_2P_2S_6$ crystals can be extended by searching for new vdW compounds of SnP_2S_6 type. New SnP_2Se_6, SnP_2Te_6, GeP_2S_6, GeP_2Se_6, and GeP_2Te_6 compounds with a layered rhombohedral structure R3 are predicted by DFT calculations [85]. Variation of electron and phonon spectra is traced for the Sn → Ge substitution in the cation sublattice and for the compounds with S, Se, or Te in the anion sublattice. A polar metal state is expected at normal pressure in a layered GeP_2Te_6 crystal. Also, the softening of the phonon spectrum and metallization were predicted [85] for the SnP_2S_6 crystal at a pressure of about 80 GPa.

References

1 Diehl, R. and Carpentier, C.D. (1978). The structural chemistry of indium phosphorus chalcogenides. *Acta Crystallogr., Sect. B: Struct. Crystallogr. Cryst. Chem.* 34 (4): 1097–1105.

2 Gave, M.A., Bilc, D., Mahanti, S.D. et al. (2005). On the lamellar compounds $CuBiP_2Se_6$, $AgBiP_2Se_6$ and $AgBiP_2S_6$. Antiferroelectric phase transitions due to cooperative Cu^+ and Bi^{3+} ion motion. *Inorg. Chem.* 44 (15): 5293–5303.

3 Ouili, Z., Leblanc, A., and Colombet, P. (1987). Crystal structure of a new lamellar compound: $Ag_{12}In_{12}PS_3$. *J. Solid State Chem.* 66 (1): 86–94.

4 Simon, A., Ravez, J., Maisonneuve, V. et al. (1994). Paraelectric–ferroelectric transition in the lamellar thiophosphate $CuInP_2S_6$. *Chem. Mater.* 6 (9): 1575–1580.

5 Maisonneuve, V., Cajipe, V., Simon, A. et al. (1997). Ferrielectric ordering in lamellar $CuInP_2S_6$. *Phys. Rev. B: Condens. Matter Mater. Phys.* 56 (17): 10860–10868.

6 Cajipe, V.B., Ravez, J., Maisonneuve, V. et al. (1996). Copper ordering in lamellar $CuMP_2S_6$ (M = Cr, In): transition to an antiferroelectric or ferroelectric phase. *Ferroelectrics* 185 (1–4): 135–138.

7 Maisonneuve, V., Reau, J.M., Dong, M., and Cajipe, V.B. (1997). Ferroelectrics ionic conductivity in ferroic $CuInP_2S_6$. *Ferroelectrics* 196 (1): 37–41.

8 Bourdon, X., Maisonneuve, V., Cajipe, V.B. et al. (1999). Copper sublattice ordering in layered $CuMP_2Se_6$ (M = In, Cr). *J. Alloys Compd.* 283 (1, 2): 122–127.

9 Vysochanskii, Y.M., Molnar, A.A., Gurzan, M.I. et al. (2000). Dielectric measurement study of lamellar $CuInP_2Se_6$: successive transitions towards a ferroelectric state via an incommensurate phase? *Solid State Commun.* 115 (1): 13–17.

10 Stock, C., Xu, G., Gehring, P.M. et al. (2007). Neutron and X-ray diffraction study of cubic [111] field-cooled $Pb(Mg_{1/3}Nb_{2/3})O_3$. *Phys. Rev. B: Condens. Matter Mater. Phys.* 76 (6): 1–11.

11 Binder, K. and Young, A.P. (1986). Spin glasses: experimental facts, theoretical concepts, and open questions. *Rev. Mod. Phys.* 58 (4): 801–976.

12 Bourdon, X. (1999). $A_2D_{31}P$ MAS NMR study of polycrystalline $Cd_3(PO_4)_2$. *Chem. Mater.* 11: 2680–2686.

13 Vysochanskii, Y.M., Stephanovich, V., Molnar, A. et al. (1998). Raman spectroscopy study of the ferrielectric–paraelectric transition in layered $CuInP_2S_6$. *Phys. Rev. B: Condens. Matter Mater. Phys.* 58 (14): 9119–9124.

14 Maisonneuve, V., Evain, M., Payen, C. et al. (1995). Room-temperature crystal structure of the layered phase $Cu(I)In(III)P_2S_6$. *J. Alloys Compd.* 218: 157–164.

15 Brec, R., Ouvrard, G., Louisy, A., and Rouxel, J. (1980). Proprietes Structurales de Phases $M^{II}PX_3$ (X = S, Se). *Ann. Chim.* 5: 499–512.

16 Klingen, W., Eulenberger, G., and Hahn, H. (1973). Uber die Kristallstrukturen von $Fe_2P_2Se_6$ und $Fe_2P_2S_6$. *Z. Anorg. Allg. Chem.* 401: 97–112.

17 Sheldrick, G.M. (2008). A short history of SHELX. *Acta Crystallogr., Sect. A: Found. Crystallogr.* 64 (1): 112–122.

18 Fagot-Revurat, Y., Bourdon, X., Bertran, F. et al. (2003). Interplay between electronic and crystallographic instabilities in the low-dimensional ferroelectric $CuInP_2Se_6$. *J. Phys.: Condens. Matter* 15 (3): 595–602.

19 Vysochanskii, Y.M., Molnar, A.A., Gurzan, M.I., and Cajipe, V.B. (2001). Phase transitions in $CuInP_2(Se_xS_{1-x})_6$ layered crystals. *Ferroelectrics* 257 (1): 147–154.

20 Macutkevic, J., Banys, J., Grigalaitis, R., and Vysochanskii, Y. (2008). Asymmetric phase diagram of mixed $CuInP_2(S_xSe_{1-x})_6$ crystals. *Phys. Rev. B: Condens. Matter Mater. Phys.* 78 (6): 1–9.

21 Banys, J., Macutkevic, J., Lapinskas, S. et al. (2006). Relaxation times of $BP_{1-x}BPI_x$ mixed crystals: atypical dipolar glass behavior of the average local potential asymmetry. *Phys. Rev. B: Condens. Matter Mater. Phys.* 73 (14): 1–11.

22 Grigalaitis, R., Banys, J., Kania, A., and Slodczyk, A. (2005). Distribution of relaxation times in PMN single crystal. *J. Phys. IV* 128: 127–131.

23 Kamba, S., Nuzhnyy, D., Veljko, S. et al. (2007). Dielectric relaxation and polar phonon softening in relaxor ferroelectric $PbMg_{1/3}Ta_{2/3}O_3$. *J. Appl. Phys.* 102 (7): 074106(1)–074106(9).

24 Blinc, R., Dolinšek, J., Gregorovic, A. et al. (1999). Local polarization distribution and Edwards–Anderson order parameter of relaxor ferroelectrics. *Phys. Rev. Lett.* 83 (2): 424–427.

25 Vysochanskii, Y.M., Beley, L., Perechinskii, S. et al. (2004). Phase transitions and disordering effects in $CuInP_2S(Se)_6$ layered ferrielectrics. *Ferroelectrics* 298: 361–366.

26 Pirc, R., Tadić, B., and Blinc, R. (1987). Random-field smearing of the proton-glass transition. *Phys. Rev. B: Condens. Matter Mater. Phys.* 36 (16): 8607–8615.

27 Kind, R., Blinc, R., Dolinsek, J. et al. (1991). Tl^{2+} EPR study of the dynamics of the proton-glass transition in $Rb_{1-x}(NH_4)_xH_2PO_4$. *Phys. Rev. B: Condens. Matter Mater. Phys.* 43 (4): 2511–2518.

28 Banys, J., Macutkevic, J., Samulionis, V. et al. (2004). Dielectric and ultrasonic investigation of phase transition in $CuInP_2S_6$ crystals. *Phase Transitions* 77 (4): 345–358.

29 Banys, J., Macutkevic, J., Brilingas, A. et al. (2005). Broadband dielectric spectroscopy of betaine phosphate$_{0.03}$ betaine phosphite$_{0.97}$ crystals in the vicinity of the ferroelectric phase transitions. *Phase Transitions* 78 (12): 869–881.

30 Trybula, Z., Schmidt, V., and Drumheller, J. (1991). Coexistence of proton-glass and ferroelectric order in $Rb_{1-x}(NH_4) \times H_2AsO_4$. *Phys. Rev. B: Condens. Matter Mater. Phys.* 43 (1): 1287(R).

31 Matsushita, E. and Takahashi, K. (2002). Relaxor behaviors in ferroelectric–antiferroelectric mixed crystals. *Jpn. J. Appl. Phys.* 41 (11): 7184–7188.

32 Korner, N., Pfammatter, C., and Kind, R. (1993). Soft mode, “relaxor”, and glassy-type dynamics in the solid solution $Rb_{1-x}(ND_4)_xD_2PO_4$. *Phys. Rev. Lett.* 70 (9): 1283–1286.

33 Maisonneuve, V., Payen, C., and Cajipe, B.V. (1995). $CuCrP_2S_6$ magnetic ordering. *J. Solid State Chem.* 116: 208–210.

34 Colombet, P., Leblanc, A., Danot, M., and Rouxel, J. (1982). Structural aspects and magnetic properties of the lamellar compound $Cu_{0.50}Cr_{0.50}PS_3$. *J. Solid State Chem.* 41 (2): 174–184.

35 Maisonneuve, V., Cajipe, V.B., and Payen, C. (1993). Low-temperature neutron powder diffraction study of $CuCrP_2S_6$: observation of an ordered, antipolar copper sublattice. *Chem. Mater.* 5 (6): 758–760.

36 Dziaugys, A., Banys, J., Macutkevic, J. et al. (2010). Dipolar glass phase in ferrielectrics: $CuInP_2S_6$ and $Ag_{0.1}Cu_{0.9}InP_2S_6$ crystals. *Phys. Status Solidi A* 207 (8): 1960–1967.

37 Maior, M.M., Motrja, S.F., Gurzan, M.I. et al. (2008). Dipole glassy state in layered mixed crystals of $Cu(In,Cr)P_2(S,Se)_6$ system. *Ferroelectrics* 376: 9–16.

38 Dziaugys, A., Shvartsman, V.V., Macutkevic, J. et al. (2012). Phase diagram of mixed $Cu(In_xCr_{1-x})P_2S_6$ crystals. *Phys. Rev. B: Condens. MatterMater. Phys.* 85 (13): 1–6.

39 Bertrand, D., Fert, A.R., Schmidt, M.C. et al. (1982). Observation of a spin glass-like behaviour in dilute system $Fe_{1-x}Mg_xCl_2$. *J. Phys. C: Solid State Phys.* 15 (25): L883–L888.

40 Mattsson, J., Kushauer, J., Bertrand, D. et al. (1996). Phase diagram and mixed phase dynamics of the dilute Ising antiferromagnet $Fe_xMg_{1-x}Cl_2$, $0.7 \le x \le 1$. *J. Magn. Magn. Mater.* 152 (1, 2): 129–138.

41 Shvartsman, V.V., Bedanta, S., Borisov, P. et al. (2008). $(Sr,Mn)TiO_3$: a magnetoelectric multiglass. *Phys. Rev. Lett.* 101 (16): 17–20.

42 Borisov, P., Hochstrat, A., Shvartsman, V.V., and Kleemann, W. (2007). Superconducting quantum interference device setup for magnetoelectric measurements. *Rev. Sci. Instrum.* 78 (10): 2–5.

43 Kleemann, W., Shvartsman, V.V., Borisov, P. et al. (2011). Magnetic and polar phases and dynamical clustering in multiferroic layered solid solutions $CuCr_{1-x}In_xP_2S_6$. *Phys. Rev. B: Condens. Matter Mater. Phys.* 84 (9): 1–8.

44 Lai, Y., Song, Z., Wan, Y. et al. (2019). Two-dimensional ferromagnetism and driven ferroelectricity in van der Waals $CuCrP_2S_6$. *Nanoscale* 11 (12): 5163–5170.

45 Trew, V.C. (1961). Additivity relationships in polar diamagnetic salts. *Trans. Faraday Soc.* 57: 223.

46 Rasch, J.C.E., Boehm, M., Ritter, C. et al. (2009). Magnetoelastic coupling in the triangular lattice antiferromagnet $CuCrS_2$. *Phys. Rev. B: Condens. Matter Mater. Phys.* 80 (10): 1–7.

47 Sykes, M.F. and Essam, J.W. (1964). Exact critical percolation probabilities for site and bond problems in two dimensions. *J. Math. Phys.* 5 (8): 1117–1127.

48 Bertrand, D., Bensamka, F., Fert, A.R. et al. (1984). Phase diagram and high-temperature behaviour in dilute system $Fe_xMg_{1-x}Cl_2$. *J. Phys. C: Solid State Phys.* 17 (10): 1725–1733.

49 Joy, P.A. and Vasudevan, S. (1992). Magnetism in the layered transition-metal thiophosphates MPS_3 (M = Mn, Fe, and Ni). *Phys. Rev. B: Condens. Matter Mater. Phys.* 46 (9): 5425–5433.

50 Bogani, L. and Wernsdorfer, W. (2008). Molecular spintronics using single-molecule magnets. *Nat. Mater.* 7: 179–186.

51 Van Slageren, J., Sessoli, R., Gatteschi, D. et al. (2002). Magnetic anisotropy of the antiferromagnetic ring [$Cr_8F_8Piv_{16}$]. *Chem. Eur. J.* 8 (1): 277–285.

52 Du, K.Z., Wang, X.Z., Liu, Y. et al. (2016). Weak van der Waals stacking, wide-range band gap, and Raman study on ultrathin layers of metal phosphorus trichalcogenides. *ACS Nano* 10 (2): 1738–1743.

53 Ressouche, E., Loire, M., Simonet, V. et al. (2010). Magnetoelectric $MnPS_3$ as a candidate for ferrotoroidicity. *Phys. Rev. B: Condens. Matter Mater. Phys.* 82 (10): 1–4.

54 Wildes, A.R., Roessli, B., Lebech, B., and Godfrey, K.W. (1998). Spin waves and the critical behaviour of the magnetization in $MnPS_3$. *J. Phys.: Condens. Matter* 10 (28): 6417–6428.

55 Jeevanandam, P. and Vasudevan, S. (1999). Magnetism in $MnPSe_3$: a layered $3d^5$ antiferromagnet with unusually large XY anisotropy. *J. Phys.: Condens. Matter* 11 (17): 3563–3570.

56 Nicolosi, V., Chhowalla, M., Kanatzidis, M.G. et al. (2013). Liquid exfoliation of layered materials. *Science* 340 (6139): 72–75.

57 Li, X., Cao, T., Niu, Q. et al. (2013). Coupling the valley degree of freedom to antiferromagnetic order. *Proc. Natl. Acad. Sci. U.S.A.* 110 (10): 3738–3742.

58 Le Flem, G. (1982). Magnetic interactions in the layer compounds MPX_3 ($M = Mn, Fe, Ni; X = S, Se$). *Solid State Commun.* 43 (5): iv.

59 Kurita, N. and Nakao, K. (1989). Band structures and physical properties of magnetic layered semiconductors MPS_3. *J. Phys. Soc. Jpn.* 58: 610–621.

60 Bernasconi, M., Marra, G.L., Benedek, G. et al. (1988). Lattice dynamics of layered MPX_3 ($M = Mn, Fe, Ni, Zn; X = S, Se$) compounds. *Phys. Rev. B: Condens. Matter Mater. Phys.* 38 (17): 12089–12099.

61 Friedel, C. (1894). Sur une nouvelle série de sulfophosphures, les thiôhypophosphates. Table des matières Comptes rendus de l'Académie des sciences. *C. R. Hebd. Séances Acad. Sci.* 119: 260.

62 Clement, R. (1980). A novel route to intercalation into layered $MnPS_3$. *J. Chem. Soc., Chem. Commun.* 14: 647–648.

63 Babuka, T., Makowska-Janusik, M., Peschanskii, A.V. et al. (2020). Electronic and vibrational properties of pure $MnPS_3$ crystal: theoretical and experimental investigation. *Comput. Mater. Sci.* 177: 109592.

64 Kurosawa, K., Saito, S., and Yamaguch, Y. (1983). Neutron diffraction study on $MnPS_3$ and $FePS_3$. *J. Phys. Soc. Jpn.* 52: 3919–3926.

65 Boerio-Goates, J., Lifshitz, E., and Francis, A.H. (1981). Electronic spectroscopy of nearly octahedrally coordinated manganese in $MnPS_3$ and $CdPS_3$ lattices. *Inorg. Chem.* 20 (9): 3019–3023.

66 Chittari, B.L., Park, Y., Lee, D. et al. (2016). Electronic and magnetic properties of single-layer MPX_3 metal phosphorous trichalcogenides. *Phys. Rev. B: Condens. Matter Mater. Phys.* 94 (18): 1–16.

67 Grasso, V., Neri, F., Perillo, P. et al. (1991). Optical-absorption spectra of crystal-field transitions in $MnPS_3$ at low temperatures. *Phys. Rev. B: Condens. Matter Mater. Phys.* 44 (20): 11060–11066.

68 Yagotintsev, K.A., Strzhemechny, M.A., Prokhvatilov, A.I. et al. (2012). Interlayer Mn–Mn exchange parameter in $MnPS_3$ from X-ray diffraction data. *Low Temp. Phys.* 38 (5): 383–385.

69 Belianinov, A., He, Q., Dziaugys, A. et al. (2015). $CuInP_2S_6$ room temperature layered ferroelectric. *Nano Lett.* 15 (6): 3808–3814.

70 Liu, F., You, L., Seyler, K.L. et al. (2016). Room-temperature ferroelectricity in $CuInP_2S_6$ ultrathin flakes. *Nat. Commun.* 7: 1–6.

71 Zhu, Z., Chen, X., Li, W., and Qi, J. (2019). Electric field control of the semiconductor–metal transition in two dimensional $CuInP_2S_6$/germanene van der Waals heterostructure. *Appl. Phys. Lett.* 114: 223102.

72 Si, M., Liao, P.Y., Qiu, G. et al. (2018). Ferroelectric field-effect transistors based on MoS_2 and $CuInP_2S_6$ two-dimensional van der Waals heterostructure. *ACS Nano* 12 (7): 6700–6705.

73 Huang, W., Wang, F., Yin, L. et al. (2020). Gate-coupling-enabled robust hysteresis for nonvolatile memory and programmable rectifier in van der Waals ferroelectric heterojunctions. *Adv. Mater.* 32 (14): 1–9.

74 Wang, X., Yu, P., Lei, Z. et al. (2019). van der Waals negative capacitance transistors. *Nat. Commun.* 10 (1): 1–8.

75 Zhao, M., Gou, G., Ding, X., and Jun, S. (2020). Ultrathin two-dimensional vertical ferroelectric tunneling junction based on $CuInP_2S_6$ monolayer. *Nanoscale* 12 (23): 12522–12530.

76 Si, M., Saha, A.K., Liao, P.Y. et al. (2019). Room-temperature electrocaloric effect in layered ferroelectric $CuInP_2S_6$ for solid-state refrigeration. *ACS Nano* 13 (8): 8760–8765.

77 Fei, Z., Zhao, W., Palomaki, T.A. et al. (2018). Ferroelectric switching of a two-dimensional metal. *Nature* 560: 336–339.

78 Ovsyannikov, S.V., Morozova, N.V., Korobeinikov, I.V. et al. (2017). Tuning the electronic and vibrational properties of $Sn_2P_2Se_6$ and $Pb_2P_2S_6$ crystals and their metallization under high pressure. *Dalton Trans.* 46 (13): 4245–4258.

79 Ondrejkovic, P., Guennou, M., Kempa, M. et al. (2013). An X-ray scattering study of $Sn_2P_2S_6$: absence of incommensurate phase up to 1 GPa. *J. Phys.: Condens. Matter* 25 (11): 115901.

80 Rushchanskii, K.Z., Vysochanskii, Y.M., and Strauch, D. (2007). Ferroelectricity, nonlinear dynamics, and relaxation effects in monoclinic $Sn_2P_2S_6$. *Phys. Rev. Lett.* 99 (20): 1–4.

81 Glukhov, K., Fedyo, K., Banys, J., and Vysochanskii, Y. (2012). Electronic structure and phase transition in ferroelectic $Sn_2P_2S_6$ crystal. *Int. J. Mol. Sci.* 13 (11): 14356–14384.

82 Maior, M.M. (2000). Effect of germanium doping on pyroelectric and piezoelectric properties of $Sn_2P_2S_6$ single crystal. *IEEE Trans. Ultrason. Ferroelectr. Freq. Control* 47 (4): 877–880.

83 Zamaraite, I., Liubachko, V., Yevych, R. et al. (2020). Quantum paraelectric state and critical behavior in $Sn(Pb)_2P_2S(Se)_6$ ferroelectrics. *J. Appl. Phys.* 128 (23): 234105.

84 Wang, Z. and Willett, R.D. (1995). Synthesis and crystal structure of SnP_2S_6. *Chem. Mater.* 7: 856–858.

85 Rushchanskii, K.Z., Vysochanskii, Y.M., Cajipe, V.B., and Bourdon, X. (2006). Influence of pressure on the structural, dynamical, and electronic properties of the SnP_2S_6 layered crystal. *Phys. Rev. B: Condens. Matter Mater. Phys.* 73 (11): 1–12.

86 Ondrejkovic, P., Kempa, M., Vysochanskii, Y. et al. (2012). Neutron scattering study of ferroelectric $Sn_2P_2S_6$ under pressure. *Phys. Rev. B: Condens. Matter Mater. Phys.* 86 (22): 1–8.